Kir6.2 is essential to maintain neurite features by modulating PM20D1-reduced mitochondrial ATP generation

Nanshan Song [a],[1], Yinquan Fang [a],[1], Hong Zhu [a], Jiaqi Liu [a], Siyuan Jiang [a], Sifan Sun [b], Rong Xu [a], Jianhua Ding [a], Gang Hu [a],[b],[**], Ming Lu [a],[c],[*]

[a] *Jiangsu Key Laboratory of Neurodegeneration, Department of Pharmacology, Nanjing Medical University, Nanjing, 211166, China*
[b] *Department of Pharmacology, Nanjing University of Chinese Medicine, Nanjing, 210023, China*
[c] *Neuroprotective Drug Discovery Key Laboratory, Department of Pharmacology, Nanjing Medical University, Nanjing, 211166, China*

ARTICLE INFO

ABSTRACT

Kir6.2, a pore-forming subunit of the ATP-sensitive potassium (KATP) channels, regulates the functions of metabolically active tissues and acts as an ideal therapeutic target for multiple diseases. Previous studies have been conducted on peripheral kir6.2, but its precise physiological roles in the central nervous system (CNS) have rarely been revealed. In the current study, we evaluated the neurophenotypes and neuroethology of kir6.2 knockout (kir6.2$^{-/-}$) mice. We demonstrated the beneficial effects of kir6.2 on maintaining the morphology of mesencephalic neurons and controlling the motor coordination of mice. The mechanisms underlying the abnormal neurological features of kir6.2 deficiency were analyzed by RNA sequencing (RNA-seq). *Pm20d1*, a gene encoding PM20D1 secretase that promotes the generation of endogenous mitochondria uncouplers *in vivo*, was dramatically upregulated in the midbrain of kir6.2$^{-/-}$ mice. Further investigations verified that PM20D1-induced increase of N-acyl amino acids (N-AAAs) from circulating fatty acids and amino acids promoted mitochondrial impairments and cut down the ATP generation, which mediated the morphological defects of the mesencephalic neurons and thus led to the behavioral impairments of kir6.2 knockout mice. This study is the first evidence to demonstrate the roles of kir6.2 in the morphological maintenance of neurite and motor coordination control of mice, which extends our understanding of kir6.2/KATP channels in regulating the neurophysiological function.

1. Introduction

ATP-sensitive potassium (KATP) channels are hetero-octamers composed of four pore-forming subunits (kir6.1 or kir6.2) and four regulatory subunits (SUR1, SUR2A or SUR2B). The channels are mainly distributed in high energy-demanding cells, including pancreatic β cells, myocardial cells, vascular smooth muscle cells, skeletal muscle cells and neuronal cells [1]. Research on KATP channels mostly focus on the peripheral tissues, whereas the precise physiological roles of KATP channels in the central nervous system (CNS) are poorly elucidated. Kir6.2, a KATP channel pore-forming subunit, is mainly expressed in neuronal populations in the brain [2]. Several studies have been conducted on the

involvement of astrocytic kir6.2 in regulating brain functions [3,4], raising concerns about the cell-specific distribution of kir6.2 in the brain. Patients with mutations in *KCNJ11*, the kir6.2-encoding gene, have been recently verified to exhibit neurological and neuropsychological abnormalities [5]. Studies have also demonstrated predominant neurological features in kir6.2 knockout (kir6.2$^{-/-}$) mice, including dysregulated neurotransmitter release and impaired motor ability [6–8]. These findings indicate that kir6.2-composed KATP channels play important but unknown roles in the biological processes of the brain.

As the executors of brain functions, neurons are highly polarized cells with a single long axon and several short but branched dendritic arbors. These morphologic characteristics are critical for central

---

information transmission via electrical activity and neurotransmitter signals [9,10]. Neurotransmitter release and electrical sensitivity maintenance are energy-demanding processes in neurons, hence the precise regulation of ATP generation via oxidative phosphorylation is significant [10]. As an acute sign of brain injury, abnormal neurite morphology is observed in neurological and psychiatric disorders [11, 12]. For example, functional synaptic connectome deficits underlie the onset of neurodegenerative diseases and are the leading cause of learning and memory impairments in the aging brain [13–15]. Therefore, remodeling the impaired neurite architecture may potentially impede neurodegeneration.

In the present study, we explored the physiological functions of kir6.2 in the CNS and confirmed that kir6.2 is mainly expressed in neurons under physiological conditions. In kir6.2$^{-/-}$ mice, we observed subtle deficits in the motor coordination and abnormal morphology of neuronal neurites in the midbrain. The underlying mechanism was analyzed by RNA sequencing (RNA-seq). PM20D1, a secreted enzyme that promotes the generation of endogenous mitochondrial uncouplers *in vivo*, was increased in the midbrain of kir6.2$^{-/-}$ mice. Further investigations *in vitro* revealed that the formation of N-acyl amino acids (N-AAAs) promoted by PM20D1 secretase mediated neuronal morphology defects by inducing mitochondrial metabolism impairment. *Pm20d1* knockdown recovered the neurite architecture abnormalities and behavioral impairments of the kir6.2 knockout mice. We additionally found diazoxide, the kir6.2/KATP channel opener, increased the expressions of neurite-related proteins and extended the neuronal processes, thus remodeling the neuronal atrophy in the aging brain. These findings elucidate the novel roles of kir6.2 in regulating the neuronal structure and brain function, which provides insights into the pathological roles of kir6.2 in brain diseases.

2. Materials and methods

2.1. Experimental animals and diazoxide treatment

Kir6.2 knockout mice (5-month old) with a body weight of 26–30 g were donated by Professor Miki (Chiba University, Japan). C57BL/6J mice (5-month old) were provided by the Comparative Medicine Center of Yangzhou University. Mice were bred and maintained in the Animal Resource Center of the Faculty of Medicine, Nanjing Medical University. They were given free access to food and water in a room with an ambient temperature of 22 °C ± 2 °C and a 12:12-h light/dark cycle. All animal experiments were approved by the review committee from Nanjing Medical University and complied with institutional guidelines.

For diazoxide administration, diazoxide (MedChemExpress, HY-B1140, NJ, USA) was dissolved in distilled water and was administered by oral administration (10 mg/kg bodyweight) every day. Distilled water-treatment was used as vehicle control. 18-month-old C57BL/6J mice, equivalent to 60-year-old humans [16], were used in this experiment. After receiving the diazoxide for two weeks, animals were sacrificed and the biochemical analysis were conducted.

2.2. Behavioral tests

2.2.1. Open field test (OFT)

The mice were acclimatized in the behavioral procedure room for 30 min. Spontaneous activities of mice were video-recorded for 5 min in a plastic cage (20 cm × 20 cm × 15 cm) with an outlined center area (10 cm × 10 cm). The mice were individually placed into the open field which was cleaned with 75% (vol/vol) ethanol to minimize olfactory cues in the experimental interval between each animal. The software Top Scan Version 2.0 was used to quantify the overall distance traveled (in cm) and running velocity (cm/seconds, cm/s) as indices of motor activity.

2.2.2. Rotarod test

The motor balance and coordination of mouse limbs were evaluated using a rotarod test. The mice were placed in a separate compartment on an accelerating rotarod rod. The mice were acclimatized in the rotating rod from 2 rpm to 25 rpm in 5 min for two times with intervals of 20 min between trials. Then, the mice were tested at 25 rpm for 3 min. The latency to fall (s) was recorded for each mouse as an indicator for motor coordination.

2.2.3. Pole test

Bradykinesia and motor performance in mice were evaluated using a pole test. The mice were placed, with their head upward, on the top of a vertical pole (rough-surfaced, measuring 1 cm in diameter and 50 cm in height). All mice were accustomed to the apparatus before the test for three times. The total time taken to reach the base of the pole until the four paws were on the ground was recorded, with 60 s as the maximum time. The results for total time (s) were recorded.

2.2.4. Novel object recognition test

The mice were placed in the open field apparatus for 5 min, with two identical objects on Day 1 (as habituation). As a recognition memory index, the time taken to explore the new object was measured on Day 2, with one familiar object replaced with one novel object. The recording time was 5 min. During the interval, the objects and the open field were cleaned with 75% (vol/vol) ethanol to minimize any olfactory cues.

2.2.5. Y-maze test

In the Y-maze tests, each mouse was placed at the center of a symmetrical Y-maze and was allowed to explore freely through the maze, except for the novel arm, for 5 min. In the formal experiment, all experimental arms, including the novel arm, were opened. Bouts of novel arm entry and duration in the novel arm were recorded. The hindpaw of a mouse entering one arm was defined as one arm entry. The total time of the experiment was 5 min.

2.3. Primary cell cultures and treatments

Primary neuron and astrocyte cultures were conducted as described in previous studies [17,18]. Primary neuron cultures were prepared from the brain tissues of C57BL/6J mice at embryonic day 16 (E16). Observed under the microscope, the meninges and blood vessels were removed, and the separated brain tissue was transferred into fresh a high-glucose Dulbecco's modified Eagle's medium (DMEM, Gibco, 12100–046, NY, USA). The tissues were digested with 0.125% trypsin (Gibco, 27250018) at 37 °C for 5 min, and terminated with 10% fetal bovine serum (FBS, Gibco, 10437028). The cell suspension was filtered with a 40 μm filter (BD falcon, 352340, NJ, USA) and centrifuged at 1000 g for 5 min. The cell precipitate was resuspended in Neurobasal medium (Gibco, 21103049) supplemented with 2% B27 (Gibco, 17504044), 1% penicillin/streptomycin (Gibco, 15640055) and 0.5 mM glutamine (Gibco, 25030081) and the seeded into cell culture dishes pre-coated with 0.1 mg/mL poly-L-lysine (Sigma, p0296, MO, USA). The medium was renewed every 3.5 d and the cells were treated on Day 7.

For primary astrocyte cultures, the brain tissues of neonatal mice aged 1–3 d were stripped of meninges and blood vessels under a microscope. The tissues were then digested with 0.25% trypsin (Gibco, 27250018) for 2 min and terminated by DMEM (Gibco, 12100–046) supplemented with 10% FBS (Gibco, 10437028). The cell suspension was filtered with a 40 μm filter (BD Falcon, 352340) and centrifuged at 1000 g for 5 min. The cells were resuspended in DMEM supplemented with 10% FBS and 1% penicillin/streptomycin (Gibco, 15640055) and then plated in culture dishes (Corning, 430167, NY, USA). The culture medium was replaced with fresh medium 24 h later and then refreshed every 3 days. After the cells grew to 90% on the 7 th-9 th day, the cells were split into culture plates as needed and harvested when adherent cells exhibited normal shapes and stable characters.

In the experiments, primary neurons were treated with N-arachiodonoyl dopamine (NA-DA, Cayman, 90057, MI, USA), N-oleoyl dopamine (NO-DA, Cayman, 10115), arachidonic acid (AA, MedChemExpress, HY-109590) with dopamine (DA, Selleck, S2529, Shanghai, China), oleic acid (OA, MedChemExpress, HY-N1446) with DA for 24 h. Cell death assay or biochemical experiments were conducted. For the brain homogenate treatment, brain tissues were lysed by PBS and then normalized after protein quantification. The brain homogenate was then filtered through a 0.22-μm filter unit and diluted to a working concentration (10%) in Neurobasal medium supplemented with B27 to culture the primary neurons for 24 h.

2.4. Lentivirus (LV) transfection

The lentiviral siRNA expression vector targeting *Pm20d1* and negative control were produced by Hanbio Technology (Shanghai, China). For transfection, the primary neurons were infected with lentivirus at a multiplicity of infection (MOI) of 100. After 12 h of transfection, the culture medium was refreshed. When confluent, the transfected neurons were passaged for further experiments.

2.5. Immunofluorescence analysis

For immunocytochemical staining, primary cells were rinsed with 0.1 M phosphate-buffered saline (PBS) and then fixed in 4% paraformaldehyde for 20 min. Cell cultures on the cell slides were blocked with 5% bovine serum albumin (BSA) in PBST (0.3% Triton X-100) and then incubated with the primary antibody at 4 °C overnight. The cells were washed with PBS and then exposed to Alexa Fluor 555 goat anti-mouse (1:1000, Invitrogen, A21422, CA, USA) or Alexa Flour 488 goat anti-rabbit (1:1000, Invitrogen, A11008) for 1 h at room temperature. After they were rinsed with PBS, the cell slides were sealed with Antifade Mountant (ProLong™ Diamond Antifade Mountant, Invitrogen, P36965) and observed under an Olympus scanning microscope (Olympus BX51, Japan).

Immunofluorescence in brain slices was detected as described in our previous study [18]. The brains were dehydrated with 20% sucrose-PBS and then 30% sucrose-PBS for 3 d respectively after they were fixed in 4% paraformaldehyde. The brain tissues were sliced into serial brain sections with a thickness of 25 μm. The sections were blocked with 10% FBS in PBST (0.3% Triton X-100) for 1 h, followed by incubation overnight with a primary antibody at 4 °C. The sections were then washed with PBS and incubated with Alexa Fluor 488 conjugated goat anti-rabbit (1:1000, Invitrogen, A11008) or Alexa Fluor 555 goat anti-mouse (1:1000, Invitrogen, A21422) for 1 h at room temperature. The sections were ultimately rinsed with PBS and then mounted onto adhesive slides. Fluorescently labeled sections were visualized with a scanning microscope (Olympus BX51, Japan). The primary antibodies used for immunofluorescent staining were as follows: mouse anti-kir6.2 antibody (1:200, Santa Cruz, sc-390104, CA, USA), rabbit anti-GFAP antibody (1:1000, Abcam, ab7206, Cambridge, UK), rabbit anti-MAP2 antibody (1:200, Proteintech, 17490-1-AP, Wuhan, China), rabbit anti-PM20D1 antibody (1:200, Biorbyt, orb555691, Cambridge, UK), and mouse anti-Tau (1:200, Santa Cruz, sc-32274),.

2.6. Western blot

Mouse brain tissues and cell culture extract lysates were quantified using the QuantiPro™ BCA Assay Kit (Sigma, 23235). 30 μg of proteins were separated by sodium dodecyl sulfate polyacrylamide gel electrophoresis and then electrophoretically transferred to polyvinylidene difluoride membranes (Millipore, IPVH00010, MA, USA). The membranes were blocked with 10% nonfat dry milk in Tris-buffered saline (20 mM Tris-HCl, 500 mM NaCl, pH 7.4) with Tween 20 (Aladdin, T104863, Shanghai, China) and then probed with the following primary antibodies overnight at 4 °C: mouse anti-GFAP (1:1000, Millipore, MAB360), rabbit anti-MAP2 (1:1000, Proteintech, 17490-1-AP), rabbit anti-NeuN (1:1000, Abcam, ab177487), mouse anti-kir6.2 (1:1000, Santa Cruz, sc-390104), mouse anti-PSD-95 (1:1000, Santa Cruz, sc-32290), mouse anti-Tau (1:1000, Santa Cruz, sc-32274), mouse anti-SYP (1:1000, Santa Cruz, sc-17750), rabbit anti-PM20D1 (1:800, Biorbyt, orb555691), rabbit anti-COXIV (1:1000, proteintech, 11242-1-AP), rabbit anti-TOMM20 (1:1000, proteintech, 11802-1-AP) and mouse anti-β-actin (1:3000, Sigma, a1978). Subsequently, the membranes were incubated with a horseradish peroxidase-conjugated goat anti-mouse secondary antibody (1:2000, Thermo Fisher, 31430, MA, USA) or a goat anti-rabbit IgG secondary antibody (1:2000, Thermo Fisher, 31460) for 1 h. After washing, the membranes were scanned using the Image Quant LAS 4000 Chemiluminescence Imaging System (GE Healthcare, FL, USA) by chemiluminescence (ECL) western blotting detection reagents Pierce™ ECL (Thermo Fisher, 32132).

2.7. Nissl staining

Nissl staining was performed as described in a previous study [17]. The sections were first rinsed with PBS and mounted onto adhesive slides. The slides were then treated with a Cresyl violet acetate solution (0.1 g of Cresyl violet, 1 mL of acetic acid in 99 mL H$_2$O) for 30 min at room temperature, followed by dehydration with a graded series of alcohol and xylene. The brain slices were observed under a stereomicroscope (Olympus BX51, Japan).

2.8. Golgi staining

Golgi staining was conducted using the FD Rapid GolgiStain™ Kit (FD Neurotechnologies, PK401, Columbia), and the brain tissues were stained in accordance with the instructions provided by the manufacturer. The brains were briefly impregnated in a chromate mixture of Solution A (potassium dichromate and mercuric chloride) and Solution B (potassium chromate) away from light for 4 weeks, with the solution renewed after the first 24 h. Subsequently, tissue slices were immersed in Solution C for 3–5 d during which period the solution was replaced after 24 h. Tissues were sectioned and then plated on gelatin-coated slides by using the additional Solution C. The tissues were then allowed to dry in ventilated dark areas for 12 h. The tissues were washed with distilled water and submerged sequentially in a diluted mixture of Solution D and Solution E (Solution D:Solution E: deionized water = 1:1:3). After they were rinsed with distilled water, the tissues were dehydrated with graded alcohols (50%, 70%, 90%, and 100% ethanol in deionized water) and then cleared with xylene. The slides were sealed and observed under a microscope (Olympus BX51, Tokyo, Japan).

2.9. Quantitative real-time reverse transcription–polymerase chain reaction (RT-PCR)

Total RNA was extracted with the Trizol reagent (Invitrogen, 15596026). Reverse transcription PCR was conducted using the TaKaRa PrimeScript RT reagent kit (Takara, RR036A, Kyoto, Japan), and real-time PCR was conducted using a QuantiTect SYBR Green PCR kit (Roche, 04913914001, Basel, Switzerland) with an ABI 7300 Fast Real-time PCR System (Applied Biosystems, CA, USA). The sequences of primers for RT-PCR analysis were as follows:

Gene	Forward Primer	Reverse Primer
Kcnj11	CCATCGGCGGGCAGAAAC	ACCAGGAAGATGCCGTTACC
gfap	CCCTGGCTCGTGTGGATTT	GACCGATACCCACTCCTCTGTC
Map2	GCCAGCCTCAGAACAAACAG	AAGGTCTTGGGAGGGAAGAAC
Mcm6	ACCAACCCAAGGTTTGGAGG	TAATGCTCTCAGCGGTCTGTT
Trim12a	CCTGTCTGTCTGAACCTGATGG	GGCTTGAACATTTTGAGCCTCT
Ucn	TCTTGCTGTTAGCGGAGCG	TCGAATATGATGCGGTTCTGC
4833420G17Rik	ATGGCGCTCTATGAGGATGAT	AGGGAGGAAGTGCCTTTTCAA
Lypd1	GGCATCGCAGCAACTTTTTG	GGGATGAGCAATCGTTGTTCAG
A330076H08Rik	GATGGATGCTCCTGAGACCTG	TGGGGATTCCCACAACATCC
Cartpt	CCCGAGCCCTGGACATCTA	GCTTCGATCTGCAACATAGCG
Serpind1	GATGCCGTTTCCCCGACAG	TCAGGACTCGGTAAAGGTTGAA
Hddc3	CCGCTCACAAACACCGACA	GCGGCCTGTAACACCACAA
Abca8a	CGTGGGCCTTATTGTGCAAGA	CAGGTCCACATCAGGCAGTG
Pm20d1	CCCCCAAAGGAGACAAGCA	TGCTTGTCTCCTTTGGGGG
Ifltd1	TCGGAGCCTCTAGCCAGTG	AGAAGTGGACTGAAGAATGCTG
Wdfy1	CATCCGAGTATGGCTGAAA	CTTTTCAGCCATACTCGGA
Fmo2	TTGTGGTGATTGGAGCAGGG	TGTTGGTAATGACAGAGCGGTAGA
Slc26a7	CCCCACCGAGAAGACATTAAGC	TGAACTGCCAACATTATCCCAG
Gm9625	CGCCAAAGCAACCAAGTCAG	ATCTGATGGGGAATGTGGACTC
Gm8730	CTCTCGCTTTCTGGAGGGTG	TGACTTGGTTGCTTTGACGGA
Mrpl48-ps	TCAGGGTTAAGGAGGAGCGT	CCCTGAGGTGTTGGTTTGATTG
gapdh	TGTAGACCATGTAGTTGAGGTCA	AGGTCGGTGTGAACGGATTTG

PCR thermal cycle parameters were as follows: 95 °C for 30 s, 40 cycles at 95 °C for 10 s, and 60 °C for 30 s, and a melting curve from 60 °C to 95 °C to ensure the amplification of a single product. The GAPDH gene was used as an endogenous control to normalize for differences in the amount of total RNA in each sample.

2.10. Agarose electrophoresis

The total RNA of primary neurons and astrocytes was extracted and reversely transcribed into cDNA. Subsequently, a 20 µL PCR reaction system was prepared with 1 µg of cDNA, 1 µL of upstream primer, and 1 µL of downstream primer, 10 µL of PCR mix, and DEPC water to 20 µL. The reaction conditions were as follows: 95 °C for 3 min; reps 40: 95 °C for 30 s, 60 °C for 30 s, 72 °C for 30 s; 72 °C for 3 min; hold at 4 °C. The primer sequence is as above. The amplified products were detected by 1% agarose gel electrophoresis.

2.11. Cell viability assay

The primary neurons were seeded in 96-well plates with a density of 40000 cells/well. After the treatment, the culture medium was removed, and a suspension consisting of 90 µL fresh culture medium and 10 µL of CCK8 solution (Beyotime, c0037, Shanghai, China) was added into each well. Cell viability was detected by absorbance at 450 nm.

2.12. Carboxypeptidase PM20D1 immunoassay

PM20D1 content was detected using the PM20D1 enzyme-linked immunosorbent assay (ELISA) Kit (CUSABIO, Q8C165, Wuhan, China) in accordance with the manufacturer protocol. For the brain tissues of kir6.2$^{-/-}$ and wide-type (WT) mice, the tissues were separated and then lysed in PBS with a 1:10 mass (mg)-to-volume (µL) ratio by using the ultrasonic homogenizer. After two freeze–thaw cycles to destroy the cell membrane, the tissue homogenate was centrifuged. The amount of protein in the supernatant was immediately quantified using the QuantiPro™ BCA Assay Kit (Sigma, 23235). PBS was added to homogenize the concentration of all samples. To determine the PM20D1 content in the supernatant of primary neurons, the supernatant was collected and centrifuged to remove the cell debris. The samples were tested immediately. The absorbance of the samples was detected using the Multiskan Spectrum (Thermo Fisher) with measurement absorbance at 450 nm and a correction wavelength at 540 nm.

2.13. Determination of ATP content

The ATP content in the midbrain was detected using the Enhanced ATP Assay Kit (Beyotime Biotechnology, S0027) in accordance with the manufacturer protocol. Tissues were lysed in the ATP lysis buffer, and the protein in each sample was homogenized with a lysis buffer after protein quantification. The ATP contents were determined using a luminometer.

2.14. Mitotracker Green

Mitotracker green (Beyotime, C1048) was used to stain the mitochondria. After the treatment, cell medium was discarded. The cells were incubated with fresh Mitotracker green solution at 37 °C for 40 min. High magnification images of mitochondrial morphology were captured under 63 × magnification using CarlZeiss LSM710 Laser scanning confocal microscope. Flow cytometric analysis were analyzed with the FCS Express software (Guava Easy Cyte™8, Millipore, United States).

2.15. Transmission electron microscopic (TEM) analysis

Mice were perfused with 2.5% glutaraldehyde and 2% paraformaldehyde. A small portion (~1 mm^3) of the midbrain from 3 WT mice and 3 kir6.2$^{-/-}$ mice was sectioned and incubated for 2 h at 4 °C in the same fixative. Specimens were postfixed in 1% osmium tetroxide, stained in aqueous uranyl acetate, and then dehydrated and embedded in epoxy resin. Ultrathin sections were stained using lead citrate and examined with transmission electron microscope. All experiments and photographs of TEM were supported by the grant from the Center of Forecasting and Analysis of Nanjing Medical University.

2.16. Oxygen consumption rates (OCR) analysis

Mitochondrial respiratory function of primary neurons was measured using the Seahorse xF96 (Agilent, CA, USA). Primary neurons were plated on Seahorse xF96 plates (20,000 cells/per well) and challenged 24 h with NA-DA or NO-DA, as well as AA or OA plus DA. Three cycles of baseline measurement of OCR were taken followed by 3 cycles of sequential measurements after injection of ATP synthase inhibitor oligomycin (1 µM), carbonyl cyanide-4-(trifluoromethoxy) phenylhydrazone (FCCP, mitochondrial respiration uncoupler, 0.5 µM), and antimycin A (Complex III inhibitor, 0.5 µM) in conjunction with

rotenone (Complex I inhibitor, 0.5 μM).

2.17. Stereotaxic adeno-associated virus (AAV) injection

Stereotaxic injection was conducted as described in a previous study [18]. The mice were anesthetized with pentobarbital sodium (1%, 45 mg/kg). PM20D1-siRNA AAV (1 μL of 1*10^12 V g/mL, Hanbio, Contract number: HH20191012RFF-AAV01) with green fluorescent protein (GFP) was microinjected bilaterally into the midbrain of matched kir6.2$^{-/-}$ and WT control mice using the following coordinates relative to the bregma: A/P −3.0 mm, R/L ± 1.3 mm, and D/V −4.5 mm. The respective controls were injected with equivalent volumes of negative control (NC) AAV with GFP. After 4 weeks, the knockdown effects of PM20D1-siRNA AAV were evaluated, and the behavior of the mice was analyzed. The animals were anesthetized, and the tissues were harvested for the subsequent bioassay.

2.18. RNA-seq analysis

WT and kir6.2$^{-/-}$ mouse midbrain tissue samples were quickly separated, and the samples were pretreated and prepared in accordance with the whole transcriptome sequencing standards. An Illumina HiSeq kit sequencing platform was used for transcriptional profiling via RNA-seq analysis following the recommendations of the manufacturer. HTSeq v0.6.1 was used to quantify gene expression. Differential expression analysis of the two groups was performed using the DESeq R package (1.10.1). The resulting P-values were adjusted using the Benjamini–Hochberg approach to controlling the false discovery rate. Genes with an adjusted P-value < 0.05 as determined by DESeq were considered as differentially expressed.

2.19. High performance liquid chromatography-mass spectrometry (HPLC-MS)

The midbrain tissues of WT and kir6.2$^{-/-}$ mice were immediately separated. A 1:1 mixture of methanol and acetonitrile was added to each sample. The samples were vortexed and ground for 6 min. The homogenate was centrifuged at 40000 g for 10 min at 4 °C. The supernatant was collected and filtered with a 0.22 μm filter membrane for sample analysis.

The composition and detection conditions of the system were as follows:

HPLC: Thermo Scientific Gamma UltiMate Gamma 3000 BioRS.

Chromatographic conditions: (1) chromatographic column, Thermo Scientific Hypersil Gold HILIC 100 × 2.1 mm, 1.9 μm; (2) flow rate, 0.3 mL/min; (3) water phase, 0.1% formic acid/water; (4) organic phase, 0.1% formic acid/acetonitrile; (5) chromatographic gradient, water phase/organic phase = 95:5 (0–2.5 min) → 5:95 (2.5–3.8 min) → 95:5 (3.8–5.0 min); (6) column temperature, 40 °C; (7) automatic sampler temperature, 8.0 °C.

The Thermo Scientific TSQ Quantum Ultra Triple Quadrupole Tandem Mass Spectrometer was used to conduct MS under the following conditions: (1) ion source, electrospray ionization source; (2) second scanning mode, positive ion scanning; (3) detection mode, selective reaction monitoring (SRM); (4) electrospray voltage, 400 V; (5) capillary temperature, 350 °C; (6) collision gas, high-purity argon; (7) sheath gas, nitrogen.

2.20. Statistical analysis

All data were represented as mean ± SEM with at least 3 independent experiments. Statistical analysis was performed using GraphPad Prism 7.0. The unpaired Student's t-test was used for comparing two independent groups. One-way ANOVA analysis of variance was used to compare multiple groups. Differences among multiple means were assessed using two-factor ANOVA followed by Tukey's post hoc test.

Differences were considered significant at $p < 0.05$.

3. Results

3.1. Kir6.2 is widely distributed in the brain areas but mainly exists in neurons

Kir6.2 is the most studied pore-forming subunit in KATP channels [1]. To explore the function of kir6.2 in the CNS, we first detected the distribution of kir6.2 in the main brain areas, including the cortex, striatum, hippocampus, and midbrain. The immunofluorescence assay (Fig. 1A) and Western blot analysis (Fig. 1B and C) revealed that kir6.2 was widely expressed in different brain regions.

It is generally believed that kir6.2 is mainly involved in the formation of neuronal KATP channels. However, kir6.2 is reported to be expressed in astrocytes as well [3]. To explore whether the expression of kir6.2 in the CNS showed specificity, we conducted the immunofluorescent analysis in different brain areas. The results showed that kir6.2 was co-localized with the neuronal marker MAP2 (Fig. 1D), rather than with the astrocytic marker GFAP (Fig. 1E) in different brain areas. We further verified the phenomenon in primary cell cultures in vitro. The immunofluorescent result consistently indicated that kir6.2 was expressed in primary neurons and rarely in astrocytes (Fig. 1F). Results of PCR and RT-PCR reinforced the finding, showing that KCNJ11, kir6.2-encoding gene, was expressed in neurons and undetectable in astrocytes (Fig. 1G and H). We further detected kir6.2 protein levels by Western blot analysis and confirmed that kir6.2 was only expressed in neurons but not in astrocytes (Fig. 1I and J). The above results, corroborating previously published RNA-seq datasets of Barres laboratory (http://www.brainrnaseq.org/) [20], indicated that kir6.2 was widely expressed in the CNS and specifically expressed in neuronal cells under physiological conditions.

3.2. Kir6.2-deficient mice manifest impaired motor coordination

A previous study has confirmed that adults with KCNJ11-mutation neonatal diabetes show deficits in working memory, coordination and motor sequencing [5]. We found previously that kir6.2$^{-/-}$ mice exhibited impaired locomotor activity [21]. Thus, we conducted a battery of behavioral tests to determine the neurobehavioral characteristics of kir6.2$^{-/-}$ mice. Deficiency of kir6.2 in kir6.2$^{-/-}$ mice was testified by immunofluorescence (Fig. S1A) and Western blot (Fig. S1B-C). The voluntary movement of mice was evaluated using the OFT, in which kir6.2$^{-/-}$ mice showed a shorter distance and lower speed compared to those of WT mice (Fig. 2A and B). Additionally, kir6.2$^{-/-}$ mice showed decreased movement ability and impaired motor coordination in the pole test and rotarod test (Fig. 2C and D). Next, the novel object recognition test was to investigate the exploratory behaviors of mice. No significant difference in exploratory behavior between the kir6.2$^{-/-}$ mice and the WT mice was seen in the novel object recognition test (Fig. 2E). We further applied the Y-maze test to measure the learning and memory ability of the kir6.2$^{-/-}$ mice (Fig. 2F). No significant difference in the bouts of novel arm entrance and the duration in the novel arm was observed between the WT and kir6.2$^{-/-}$ mice (Fig. 2G), implying that the kir6.2$^{-/-}$ mice showed normal learning and memory ability. Nonetheless, compared with the WT mice, the kir6.2 knockout mice traveled a shorter distance and moved at a lower speed in the Y-maze test (Fig. 2H). Taken together, these results suggested autonomous movement and motor coordination were impaired in the kir6.2$^{-/-}$ mice.

3.3. Deletion of kir6.2 induces abnormal neurite morphology in the midbrain

Given that dopaminergic neurons in the nigrostriatal system regulate motor control and spontaneous movement [22], we speculated that the
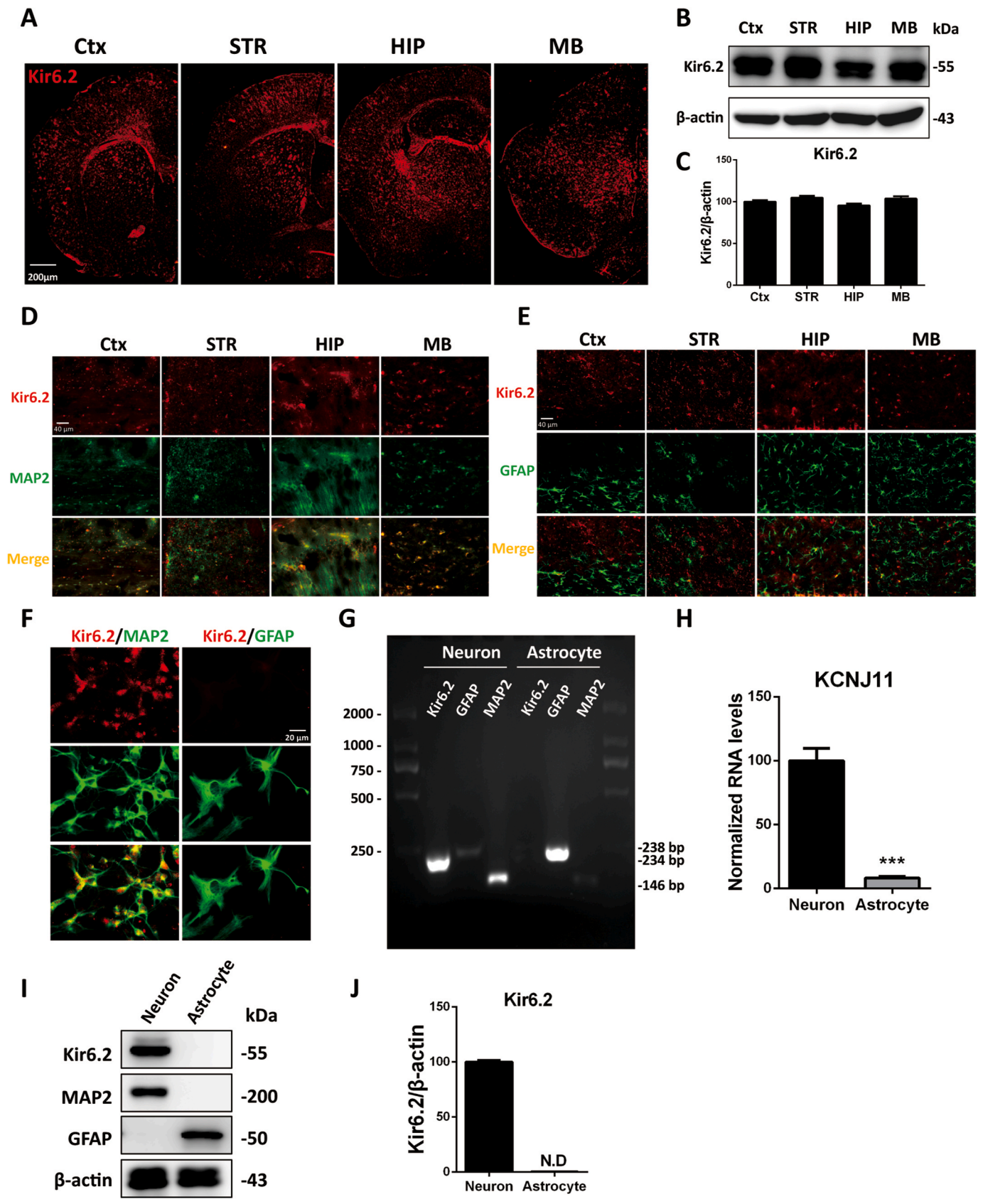
(caption on next page)

Fig. 1. Kir6.2 is widely distributed in main brain areas but mainly exists in neurons.

(A) Expressions of kir6.2 in four main brain areas including cortex (Ctx), striatum (STR), hippocampus (HIP), and midbrain (MB) analyzed by immunofluorescence staining. Scale bar is 200 μm. (B) Protein expression of kir6.2 in four main brain areas, detected by immunoblots. (C) Quantitative analysis of kir6.2 protein levels in B. Data are represented as % and analyzed using one-way ANOVA. (D) Immunofluorescence staining of kir6.2 (red) and neuronal marker MAP2 (green) in Ctx, STR, HIP and MB of healthy mice. Scale bar represents 40 μm. (E) Immunofluorescence staining of kir6.2 (red) and astrocytic marker GFAP (green). Scale bar represents 40 μm. (F) Primary cell cultures labeled with kir6.2 (red) and MAP2 (green) in primary neurons, or kir6.2 (red) and GFAP (green) in primary astrocytes. Scale bar is 20 μm. (G) Gene expression levels of *KCNJ11* in primary neurons and astrocytes analyzed by PCR in agarose electrophoresis. (H) *KCNJ11* mRNA in neurons and astrocytes detected by RT-PCR. Data are analyzed by unpaired Student's test. ***P < 0.001 *vs.* the Neuron group. (I) Expression levels of kir6.2, MAP2, and GFAP in primary neurons and astrocytes, detected by immunoblotting analysis. (J) Densitometric analysis of kir6.2 in I. Data are represented as % and analyzed by unpaired Student's test. N.D means not determined. Values are presented as means ± SEM from three independent experiments. . (For interpretation of the references to color in this figure legend, the reader is referred to the Web version of this article.)

deficits in motor coordination of kir6.2$^{-/-}$ mice might be attributable to structural or biochemical changes in the nigrostriatal system. We therefore observed the brain structures between the two genotypes of mice using Nissl staining to display the basic neural structure of the brain and Golgi staining to observe the subtle structures of neurons. We found that midbrain structure was similar between WT and kir6.2 knockout mice in Nissl staining (Fig. 3A). However, the kir6.2$^{-/-}$ mice showed decreased neurite density in the midbrain, as observed from the representative photomicrographs obtained by Golgi staining (Fig. 3B). The two-dimensional map of neurites drawn using the Image J software showed that neuronal processes in the midbrain of the kir6.2$^{-/-}$ mice were shortened and sparse with 77% of the average length of the WT neurites (Fig. 3C and D). Moreover, ultrastructures of neurites were observed under oil microscope (Fig. 3C down) and compared with WT mice, the number of dendritic spines was reduced approximately 22% in the midbrain of the kir6.2$^{-/-}$ mice (Fig. 3E). The above results indicated that kir6.2 knockout resulted in an abnormal morphology of neurons in the midbrain.

Next, we determined the expression of neurite-related markers, including Tau as an axonal marker, MAP2 as a neuronal dendritic marker, SYP as a presynaptic marker, and PSD95 as a postsynaptic marker in the WT and kir6.2$^{-/-}$ mice by western blotting analysis. The levels of synapse-related markers were significantly downregulated, which further implied neurite thinning in the midbrain of the kir6.2$^{-/-}$ mice (Fig. 3F and G). Nonetheless, no significant difference of the neuronal nuclear marker Neun was found between the WT and kir6.2$^{-/-}$ mice, implying that changes in the levels of neurite-related markers were not caused by reductions in the number of neurons. Overall, these results indicated that kir6.2 knockout led to the shortening of neuronal processes and a decrease in dendritic spine density.

3.4. The expression and activity of PM20D1 are increased in the midbrain of kir6.2-deficient mice

To dissect the mechanistic factors contributing to the abnormal neurophenotypes and neuroethology of the kir6.2$^{-/-}$ mice, we separated mesencephalic samples from the WT and kir6.2$^{-/-}$ mice and conducted RNA-seq and subsequent quantitative PCR analysis. The RNA-seq results showed that 11 genes were significantly upregulated, and 7 genes were significantly downregulated (*P*-value < 0.05) in the midbrain of the kir6.2$^{-/-}$ mice relative to those of the WT mice (Fig. 4A). The RT-PCR analysis revealed that *Pm20d1* showed a 2.64-fold increase in the kir6.2$^{-/-}$ mice (Fig. 4B), consistent with the RNA-Seq data. Western blot (Fig. 4C and D) and immunofluorescence analysis (Fig. 4E) revealed that PM20D1 was upregulated in the midbrain of the kir6.2$^{-/-}$ mice. We also conducted ELISA to determine the PM20D1 content in the midbrain homogenate. It was shown that the PM20D1 level was significantly higher in the midbrain of the kir6.2$^{-/-}$ mice than that of the WT mice (Fig. 4F). PM20D1 is a secreted enzyme that catalytically condenses free amino acids and free fatty acids to generate N-AAAs. These metabolites are endogenous mitochondrial uncouplers which promote oxidative metabolism to generate heat energy and reduce ATP production [23,24]. We detected the ATP content in the midbrain of WT and kir6.2$^{-/-}$ mice, and found that kir6.2 deletion

reduced the ATP level (Fig. 4G). As the mitochondria are the power-houses of cells to produce ATP, we next measured the mitochondrial mass by transmission electron microscope (TEM) image analysis. The results demonstrated a 15.7% reduction in mitochondrial number, and a 29.8% increase in mitochondrial size in the midbrain of kir6.2$^{-/-}$ mice compared with those from WT mice (Fig. 4H–J). We also observed more autophagic vesicles in electron microscopy images of the midbrain of kir6.2$^{-/-}$ mice (Fig. 4H, autophagic vesicles were marked with * in yellow color). Accompanying the reduced mitochondrial mass was the decreased expression of mitochondrial markers including COXIV and TOMM20 (Fig. 4K-L). These results implied that reduced mitochondrial mass and swollen mitochondrial morphology were implicated in kir6.2$^{-/-}$ midbrain, which may be induced by increased mitophagy in midbrain to facilitate the clearance of dysfunctional mitochondria. Currently, approximately 50 types of N-AAAs exist in rodent brain tissues, and the most well-studied N-AAAs generated by dopamine as a substrate in the midbrain include NO-DA and NA-DA [25,26]. NO-DA and NA-DA levels in the midbrain were thus analyzed by HPLC-MS, showing that the NO-DA and NA-DA contents in the midbrain of the kir6.2$^{-/-}$ mice increased significantly relative to those of the WT mice (Fig. 4M). The above results indicated that kir6.2 deletion led to reduced mitochondrial number and less ATP production through increasing the levels of PM20D1 and mitochondrial uncoupling agents including NO-DA and NA-DA in the midbrain of mice.

3.5. NO-DA and NA-DA impair the process of primary neurons via energy depletion

Neurons are mitochondria-dependent cells, given their high-energy demands; thus, they are particularly susceptible to mitochondrial dysfunction, particularly ATP shortage [27]. As increased N-AAA levels and decreased ATP production were seen in the midbrain of the kir6.2$^{-/-}$ mice, we then explored *in vitro* whether energy depletion induced by N-AAAs would impair the architecture of neurons. We cultured mesencephalic primary neurons from WT mice and treated the neurons with diluted midbrain homogenate from WT and kir6.2$^{-/-}$ mice to assess the roles of kir6.2 deficiency in mesencephalic neurites. No significant difference was found in the viability of mesencephalic primary neurons treated with brain homogenate from WT and kir6.2$^{-/-}$ mice (Fig. 5A). However, the midbrain homogenate from the kir6.2$^{-/-}$ mice impaired neurites, as manifested in the immunofluorescent staining of the axonal marker Tau and the dendrite marker MAP2 (Fig. 5B). Similarly, the protein levels of Tau, MAP2, SYP, and PSD-95 in primary neurons were decreased significantly after the stimulation of midbrain homogenate from the kir6.2$^{-/-}$ mice, compared with neurons treated with WT midbrain homogenate (Fig. 5C and D). The above results confirmed *in vitro* that kir6.2 deficient mice brain contained molecules that impaired mesencephalic neurites.

To explore whether NO-DA and NA-DA injured primary neuronal neurites, we subsequently exposed primary neurons with NO-DA and NA-DA. The two molecules caused no effect on cell viability in the 0.1–2 μM concentration range but reduced the ATP content at 2 μM (Fig. 5E and F). We additionally determined the mitochondrial respiration of primary neurons in response to NO-DA and NA-DA (2 μM) using
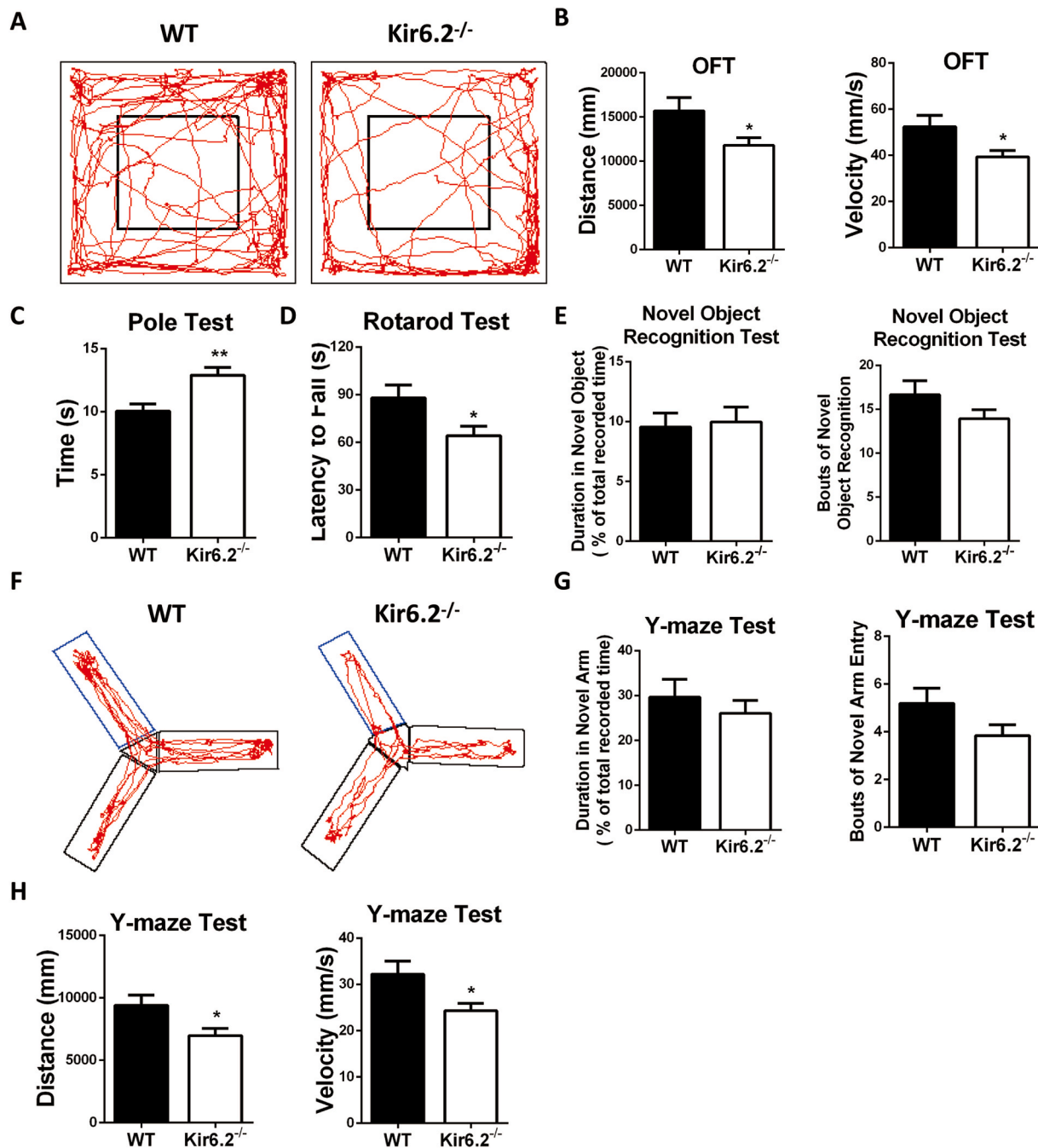

Fig. 2. Kir6.2-deficient mice show impaired motor coordination.

(A) Movement trace diagrams (red curve) of WT and Kir6.2$^{-/-}$ mice in the OFT. (B) Statistical charts of movement distance and moved speed in the OFT. (C) Analysis of the time consumed for pole climbing. (D) Analysis of latency time in the rotarod test. (E) Duration in delineated area of the novel object and bouts of novel object exploration in the novel object recognition test. (F) Movement trace diagrams (red curve) of the WT and Kir6.2$^{-/-}$ mice in the Y-maze test (the blue box indicates the novel arm). (G) Statistical charts of the duration in the novel arm and bouts of the novel arm entrance in the Y-maze test. (H) Movement distance and velocity in the Y-maze test were shown. Data are analyzed using unpaired Student's t-test. *$P < 0.05$ and **$P < 0.01$ vs. the WT group. Values are means ± SEM from 12 to 14 mice per group. . (For interpretation of the references to color in this figure legend, the reader is referred to the Web version of this article.)

Seahorse extracellular flux analysis (Fig. 5G). The OCR results showed that both NO-DA and NA-DA at 2 μM significantly reduced both basal oxygen consumption and ATP production in primary neurons (Fig. 5G and H). As we observed the reduced mitochondrial mass together with ATP depletion in kir6.2-deficent midbrain, we predicted that the reduced basal oxygen consumption after NO-DA and NA-DA treatment may result from mitochondrial number loss. Therefore we additionally assessed mitochondrial mass by both fluorescent and flow cytometric analysis of Mitotracker Green to verify our hypothesis. As shown in

Fig. 5I, healthy mitochondria in control group were in tubular or circular shapes, while NA-DA or NO-DA treatment shaped the mitochondria to be dotted patterns. Flow cytometric analysis showed that the green fluorescent intensities were decreased significantly after NA-DA or NO-DA treatment (Fig. 5J and K). These results demonstrate that NO-DA and NA-DA induce mitochondrial defects, leading to mitochondrial respiratory decline. Moreover, Western blot analysis indicated that NO-DA and NA-DA decreased the expression of neurite-related markers; NO-DA and NA-DA with concentration of 2 μM particularly showed
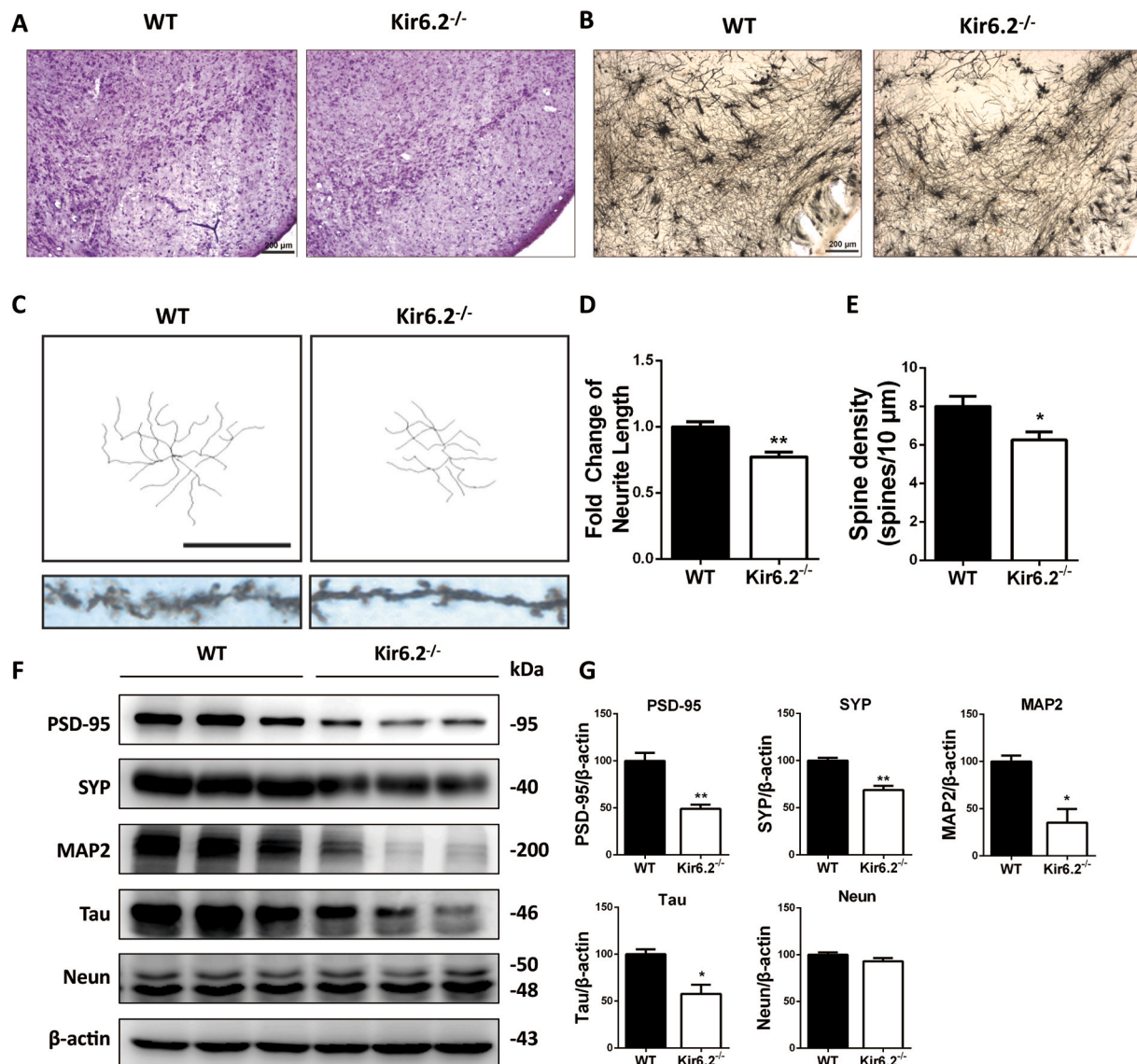
8

Fig. 3. Deletion of kir6.2 induces abnormal neurite morphology in the midbrain.
(A) Brain structures between the WT and kir6.2$^{-/-}$ mice, analyzed by Nissl staining. Scale bar is 200 μm. (B) The representative photomicrographs of Golgi staining in midbrain from the WT and kir6.2$^{-/-}$ mice. Scale bar is 200 μm. (C) Neuronal morphology reflected in a two-dimensional map drawn using the Image J software with the NeuronJ plugin (up). Scale bar is 200 μm. Dendritic spines photographed by oil microscope under 100x magnification (down). (D–E) Quantitative analysis of the average length of neuronal processes and the levels of spine density. (F) Immunoblots analysis of the neuronal marker Neun and neurite-related markers, including Tau, MAP2, SYP and PSD95 in the lysates of four main brain areas from the WT and Kir6.2$^{-/-}$ mice. (G) Densitometric analysis of kir6.2, Neun and neurite related markers in F. Data are represented as % and analyzed using unpaired Student's t-test. *P < 0.05 and **P < 0.01 *vs.* The WT group. Values are presented as means ± SEM from three independent experiments.

statistical differences (Fig. 5L-M). Meanwhile, immunofluorescence analysis of Tau and MAP2 (Fig. 5N) indicated that NO-DA and NA-DA with concentrations of 2 μM led to decreases in neurites.

Next, we treated mesencephalic primary neurons with mitochondrial uncoupler FCCP to verify the role of mitochondrial uncoupling-induced ATP shortage in neuronal neurites. We used different concentrations of FCCP to detect its effects on cell viability and ATP contents in primary neurons (Fig. S2A-B). Neurite injury, manifested as the reduced expression of neurite-related markers, was induced by FCCP with non-apoptotic concentration (Fig. S2C-D). Consistently, FCCP shortened the neurites morphology in primary neuron cultures (Fig. S2E). These *in vitro* results collectively confirmed that increased NO-DA and NA-DA in the midbrain of kir6.2$^{-/-}$ mice shortened the neurites in primary neurons via reducing mitochondrial number and ATP shortage.

3.6. Kir6.2 deletion promotes PM20D1-dependent neurite abnormalities in vitro

To verify the role of PM20D1 in kir6.2 deletion-induced neuro-phenotypes, we cultured the primary mesencephalic neurons from the WT and kir6.2$^{-/-}$ mice. Neurons from the kir6.2$^{-/-}$ mice expressed higher PM20D1 levels in both cell lysates and cell supernatants, as detected by Western blot analysis (Fig. 6A and B) and ELISA assay (Fig. 6C). It is reported that generation of endogenous N-AAAs is the condensation reaction of free fatty acids and free amino acids in circulation [24]. We subsequently treated the primary neurons from the WT and kir6.2$^{-/-}$ mice with AA or OA plus DA, and detected the generation of NA-DA and NO-DA in the supernatant of kir6.2$^{-/-}$ primary neurons. The results from HPLC/MS showed the spectra and retention time of NA-DA and NO-DA (Fig. S3A-B). Then we determined the levels of
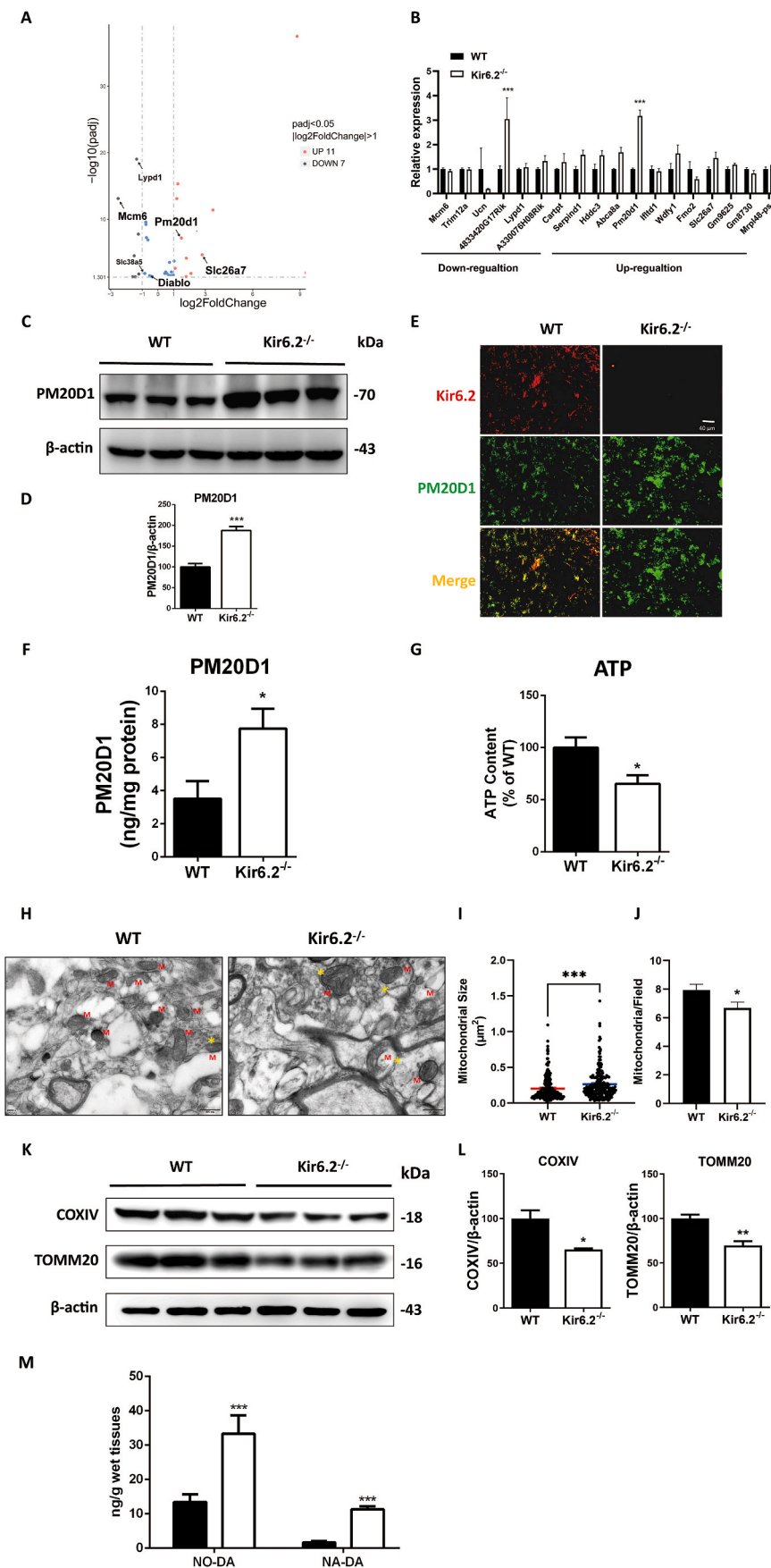
Fig. 4. The expression and activity of PM20D1 are increased in the midbrain of kir6.2-deficient mice.

(A) Volcano plot of gene expression with a significant fold change in the midbrain of the WT and kir6.2$^{-/-}$ mice, analyzed by RNA-seq. (B) Altered genes in RNA-seq between the WT and kir6.2$^{-/-}$ mice verified by real-time PCR. Data are analyzed using two-way ANOVA. ***$P <$ 0.001 *vs.* WT group. (C) Western blot analysis of PM20D1 protein expression in the midbrain of the WT and kir6.2$^{-/-}$ mice. (D) Densitometric analysis of PM20D1 protein levels was conducted in C. Data are represented as % and analyzed by the unpaired Student's t-test. ***$P < 0.001$ *vs.* WT group. (E) Immunofluorescence staining of PM20D1 (green) and kir6.2 (red) in midbrain slices of the WT and kir6.2$^{-/-}$ mice observed by microscopy. Scale bar is 40 μm. (F) The protein level of PM20D1 in midbrain homogenates of WT and kir6.2$^{-/-}$ mice was determined by ELISA kit. Data are analyzed by unpaired Student's test. *$P < 0.01$ *vs.* WT group. (G) ATP contents in the midbrain of the WT and kir6.2$^{-/-}$ mice. Data are analyzed by unpaired Student's test. *$P < 0.01$ *vs.* WT group. (H) Representative TEM image of mitochondria (marked with M in red color) and autophagic vesicles (marked with * in yellow color). (I) TEM image analysis of mitochondrial size in WT and kir6.2$^{-/-}$ midbrain. (n = 30 fields from 3 WT mice and 29 fields from 3 kir6.2$^{-/-}$ mice). (J) TEM image analysis of mitochondrial number in WT and kir6.2$^{-/-}$ midbrain. (n = 30 fields from 3 WT mice and 29 fields from 3 kir6.2$^{-/-}$ mice). Data are analyzed by unpaired Student's t-test for I and J. *$P < 0.05$ and ***$P < 0.001$ *vs.* WT group. (K) Western blot analysis of COXIV and TOMM20 in midbrain lysates from WT and kir6.2$^{-/-}$ mice. (L) Densitometric analysis of COXIV and TOMM20 protein levels. Data are represented as % and analyzed by unpaired Student's t-test. *$P < 0.05$ and **$P < 0.01$ *vs.* WT group. (M) HPLC-MS detection of NO-DA and NA-DA levels in the midbrain of the WT and kir6.2$^{-/-}$ mice. Data are analyzed using two-way ANOVA. ***$P < 0.001$ *vs.* WT group. Values are presented as means $\pm$ SEM from three mice. . (For interpretation of the references to color in this figure legend, the reader is referred to the Web version of this article.)
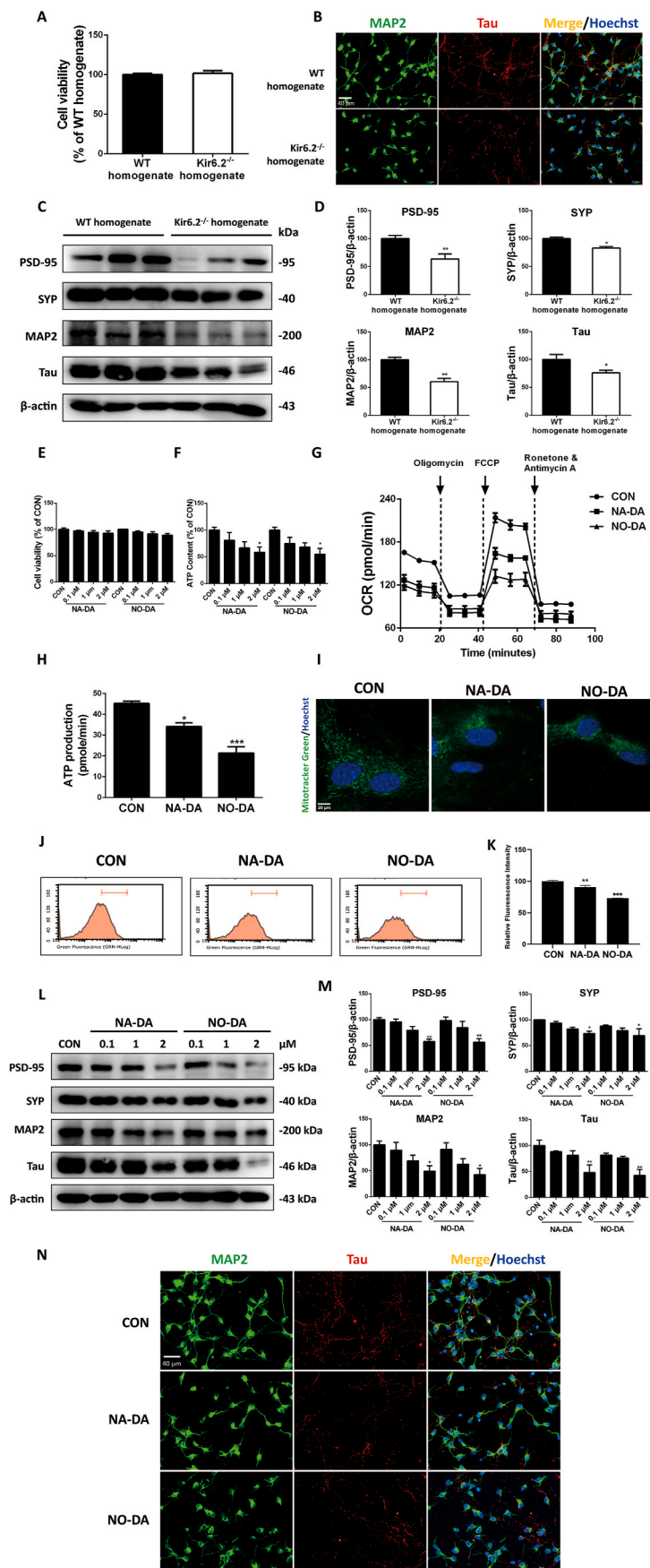
Fig. 5. NO-DA and NA-DA impair the process of neurons via energy depletion.

Primary neurons were stimulated with diluted brain homogenates from the WT and kir6.2$^{-/-}$ mice for 24 h in A-D. (A) Cell viability of primary neuron cultures were detected using the CCK8 kit. (B) Representative immunofluorescence images of MAP2 (green) and Tau (red) in primary neurons. Scale bar is 40 μm. (C) Western blot analysis of the expression of neurite-related markers, including PSD95, SYP, MAP2, and Tau. (D) Densitometric analysis of PSD95, SYP, MAP2, and Tau in C. Data are represented as % and analyzed using unpaired Student's t-test for A and D. *$P < 0.05$ and **$P < 0.01$ *vs.* WT homogenate group. Primary neurons were stimulated with concentration gradients of NA-DA and NO-DA for 24 h in E-F. (E) Cell viability of primary neurons stimulated with NA-DA and NO-DA. (F) Determination of ATP contents in neurons with NA-DA and NO-DA stimulation. (G) OCR changes in primary neurons treated with NA-DA and NO-DA were determined by the Seahorse XF analyzer, following the injection of oligomycin, FCCP, and rotenone/antimycin A. (H) Quantification of ATP production in OCR analysis of G. (I) Representative images of Mitotracker Green in primary neurons under CarlZeiss LSM710 Laser scanning confocal microscope. Scale bar is 20 μm. (J) Neurons were stained with Mitotracker Green fluorescent probe and analyzed by flow cytometry. (K) Quantification of the fluorescent intensity of Mitotracker Green. Data are analyzed using one-way ANOVA. (L) Protein expression levels of PSD-95, SYP, MAP2, and Tau, detected by immunoblotting analysis in primary neurons after NA-DA and NO-DA stimulation. (M) Densitometric analysis of PSD-95, SYP, MAP2, and Tau in L. Data are represented as %. (N) Representative immunofluorescent images of dendritic markers MAP2 (green), axonal marker Tau (red) and nuclei marker Hoechst (blue) in primary neurons stimulated with NA-DA and NO-DA were presented. Scale bar represents 40 μm. Data are analyzed using one-way ANOVA for E, F, H, K and M. *$P < 0.05$, **$P < 0.01$ and ***$P < 0.001$ *vs.* CON group. Values are means ± SEM from three independent experiments. . (For interpretation of the references to color in this figure legend, the reader is referred to the Web version of this article.)
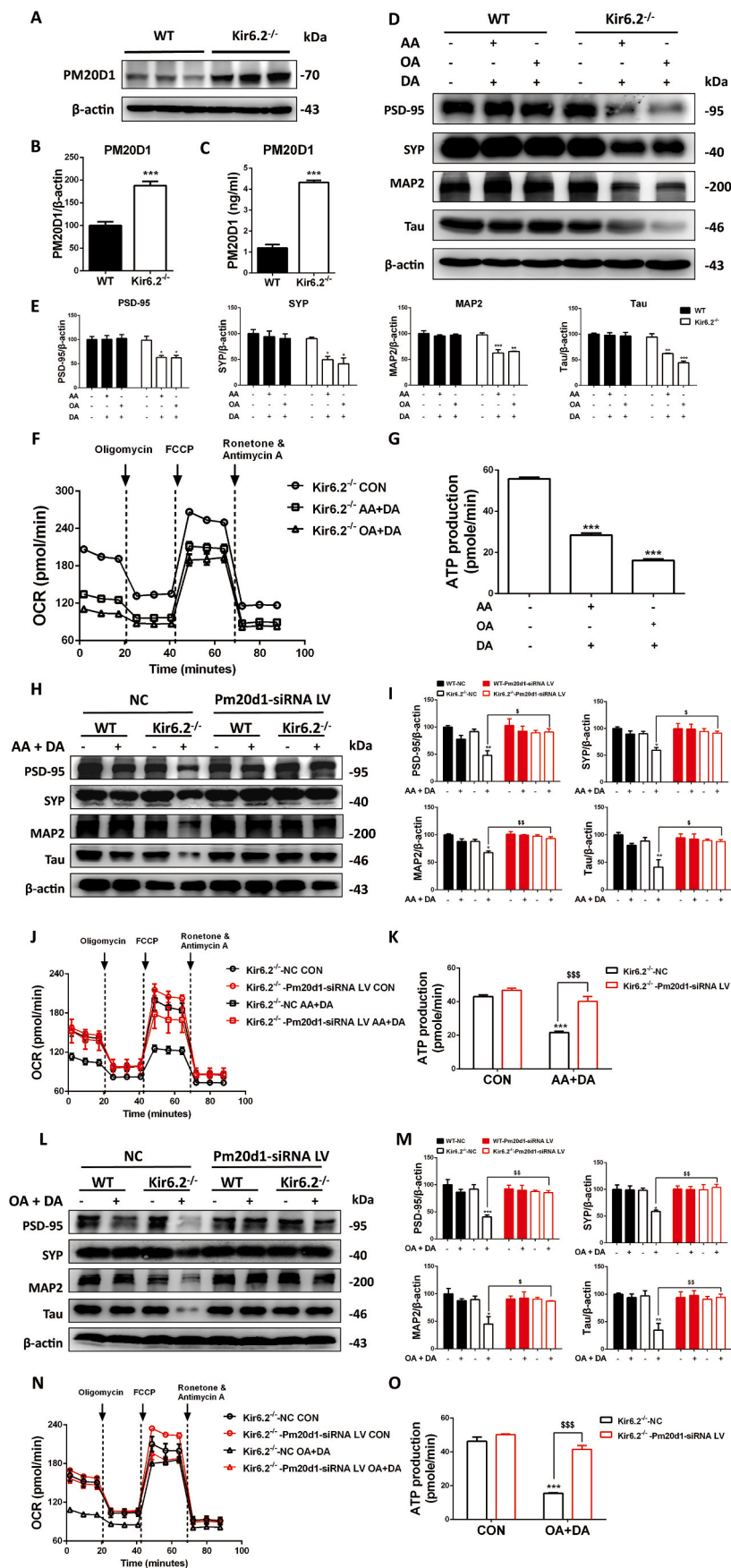
Fig. 6. Kir6.2 deletion promotes PM20D1-dependent neurite abnormalities *in vitro*.

(A) Western blot analysis of PM20D1 in primary neuron lysates from WT and kir6.2$^{-/-}$ mice. (B) Densitometric analysis of PM20D1 protein levels. Data are represented as %. (C) PM20D1 secretase content in the cell supernatant of the WT and kir6.2$^{-/-}$ mouse primary neurons, determined using the ELISA kit. Data are analyzed by unpaired Student's t-test for B and C. ***$P < 0.001$ *vs.* WT group. Primary neurons in the midbrain of the WT and kir6.2$^{-/-}$ mice stimulated with OA + DA and AA + DA for 24 h in D-G. (D) Immunoblotting analysis of neurite related markers including PSD95, SYP, MAP2, and Tau were detected in WT and kir6.2$^{-/-}$ primary neurons treated with AA + DA and OA + DA for 24 h. (E) Densitometric analysis of PSD-95, SYP, MAP2, and Tau in D. Data are represented as % and analyzed using two-way ANOVA. *$P < 0.05$, **$P < 0.01$ and ***$P < 0.001$ *vs.* CON group of the same genotype. (F) OCR changes in kir6.2$^{-/-}$ primary neurons treated with OA + DA or AA + DA were determined by the Seahorse XF analyzer, following the injection of oligomycin, FCCP, and rotenone/antimycin A. (G) Quantification of ATP production in OCR analysis of F. Data are analyzed by one-way ANOVA. ***$P < 0.001$ *vs.* kir6.2$^{-/-}$ CON group. Primary neurons in the midbrain of the WT and kir6.2$^{-/-}$ mice transfected with NC and *Pm20d1*-siRNA LV for PM20D1 knockdown and then stimulated with OA + DA or AA + DA for 24 h in H-O. (H) Immunoblotting analysis of neurite related markers including PSD95, SYP, MAP2, and Tau in primary neurons. (I) Densitometric analysis of PSD-95, SYP, MAP2, and Tau in H. Data are represented as % and analyzed by two-way ANOVA. *$P < 0.05$ and **$P < 0.01$ *vs.* kir6.2$^{-/-}$-NC group. $^{\$}P < 0.05$ and $^{\$\$}P < 0.01$ *vs.* kir6.2$^{-/-}$-NC AA + DA group. (J) OCR changes in kir6.2$^{-/-}$ primary neurons were determined by the Seahorse XF analyzer, following the injection of oligomycin, FCCP, and rotenone/antimycin A. (K) Quantification of ATP production in OCR analysis of J. Data are represented as % and analyzed by two-way ANOVA. ***$P < 0.001$ *vs.* kir6.2$^{-/-}$-NC group. $^{\$\$\$}P < 0.001$ *vs.* kir6.2$^{-/-}$-NC AA + DA group. (L) Immunoblotting analysis of neurite related markers including PSD95, SYP, MAP2, and Tau in primary neurons. (M) Densitometric analysis of PSD-95, SYP, MAP2, and Tau. Data are represented as % and analyzed using two-way ANOVA. *$P < 0.05$ and **$P < 0.01$ *vs.* kir6.2$^{-/-}$-NC group. $^{\$}P < 0.05$ and $^{\$\$}P < 0.01$ *vs.* kir6.2$^{-/-}$-NC OA + DA group. (N) OCR changes in kir6.2$^{-/-}$ primary neurons were determined by the Seahorse XF analyzer, following the injection of oligomycin, FCCP, and rotenone/antimycin A. (O) Quantification of ATP production in OCR analysis of N. Data are analyzed by two-way ANOVA. ***$P < 0.001$ *vs.* kir6.2$^{-/-}$-NC group. $^{\$\$\$}P < 0.001$ *vs.* kir6.2$^{-/-}$-NC OA + DA group. Values are means ± SEM from three independent experiments.
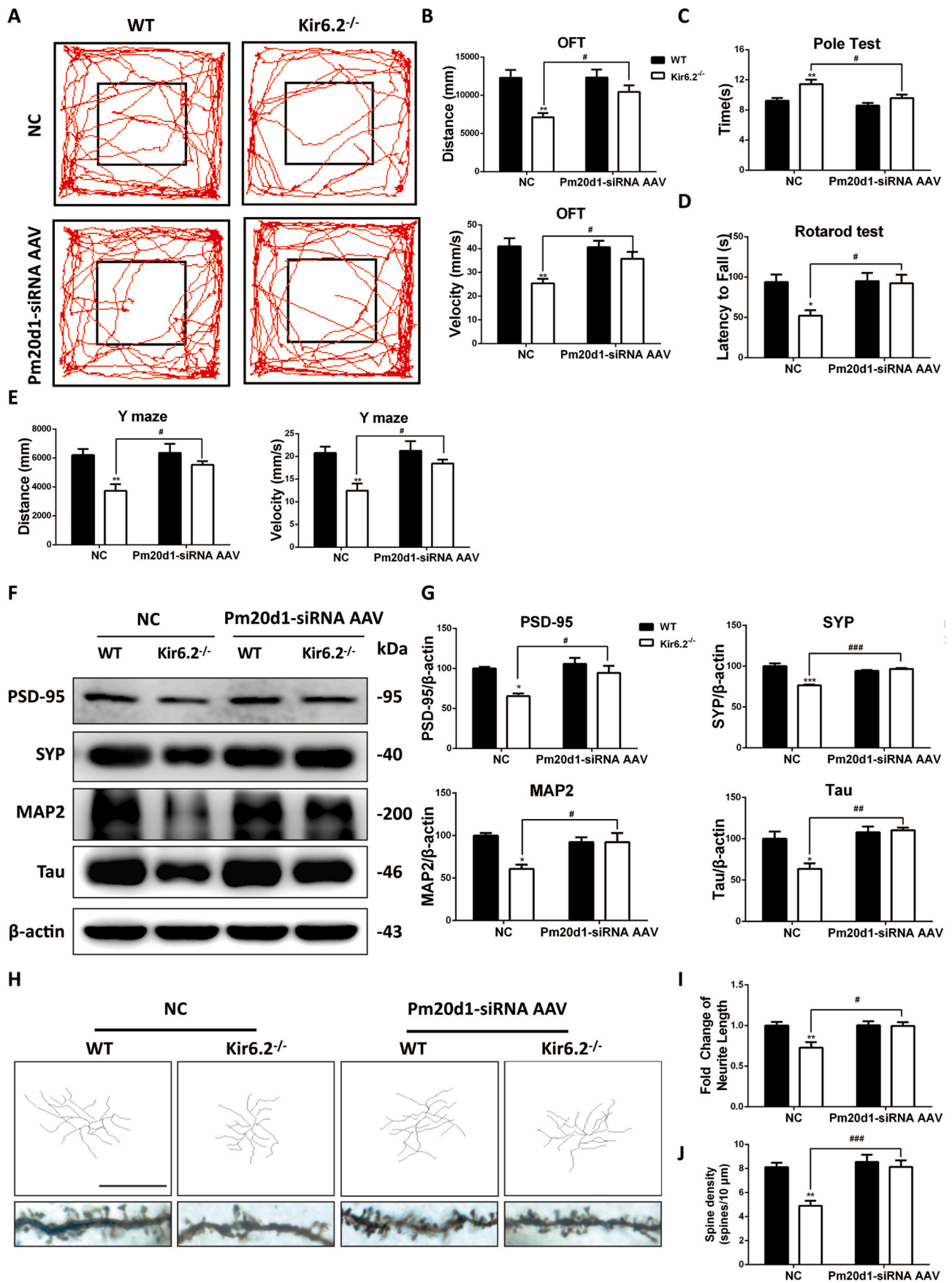
(caption on next page)

Fig. 7. *Pm20d1* knockdown recovers neuronal process abnormality and motor disability in kir6.2$^{-/-}$ mice.
(A) Movement tracking diagrams (red curve) of the WT and Kir6.2$^{-/-}$ mice with *Pm20d1*-AAV and empty vector injection in the OFT. (B) Statistical charts of movement distance and moved speed in the OFT. (C) Time consuming for pole climbing in pole test. (D) Analysis of the moved latency time in the rotarod test. (E) Statistical charts of the movement distance and velocity in the Y-maze test. (F) Western blot analysis of the expression levels of neuronal processes markers, including PSD-95, SYP, MAP2, and Tau. (G) Densitometric analysis of PSD-95, SYP, MAP2, and Tau in F. Data are represented as %. (H) A two-dimensional map of neuronal morphology in the midbrain of WT and kir6.2$^{-/-}$ mice injected with Pm20d1-siRNA AAV and empty vector (up). Scale bar is 200 μm. Dendritic spines in midbrain photographed by an oil microscope under 100x magnification (down). (I) Quantitative analysis of the average length of processes. (J) Quantitative analysis of spine density. Statistical analysis conducted by two-way ANOVA. *$P < 0.05$, **$P < 0.01$ and ***$P < 0.001$ *vs.* the WT-NC group, $^{\#}P < 0.05$, $^{\#\#}P < 0.01$ and $^{\#\#\#}P < 0.001$ *vs.* the kir6.2$^{-/-}$-NC group. Values are means ± SEM from three independent experiments. . (For interpretation of the references to color in this figure legend, the reader is referred to the Web version of this article.)

neuronal process markers and observed the neurite morphology. Treatment with AA + DA and OA + DA significantly downregulated these protein levels of neurite-related markers in the kir6.2$^{-/-}$ neurons rather than in WT neurons (Fig. 6D and E). Our OCR results showed that AA + DA and OA + DA significantly reduced ATP production in kir6.2$^{-/-}$ primary neurons (Fig. 6F and G), but not in WT neurons (Fig. S3C-D). Moreover, *Pm20d1* knockdown was implemented using the *Pm20d1*-siRNA lentivirus in primary neurons. We found that *Pm20d1* knockdown recovered the reduction in the protein level of neurite-related markers in kir6.2-deficient neurons stimulated with AA + DA (Fig. 6H and I) and OA + DA (Fig.6L–M). The decreased ATP levels in kir6.2-deficient neurons induced by AA + DA (Fig. 6J and K) and OA + DA (Fig. 6N and O) was recovered by *Pm20d1* knockdown in OCR results. Thus, kir6.2 deficiency increased the level of PM20D1 secretase, which catalyzed the condensation reactions of AA + DA and OA + DA to induce neurite abnormalities.

3.7. *Pm20d1 knockdown recovers neuronal process abnormality and motor disability in kir6.2 knockout mice*

To investigate the roles of PM20D1 in regulating the morphology of neurons and motor ability of mice, a *Pm20d1* knockdown AAV expressing a GFP was stereotactically injected into the midbrain of the WT and kir6.2$^{-/-}$ mice. The structure of *Pm20d1*-siRNA AAV was shown in Fig. S4A. The schematic diagram of the AAV injection and the representative image were presented in Fig. S4B. The knockdown efficiency of *Pm20d1*-siRNA AAV was evaluated by Western blot (Fig. S4C-D). Motor and coordination behavioral tests were performed, and we found that the motor impairments were significantly recovered in the kir6.2$^{-/-}$ mice after the *Pm20d1*-siRNA AAV injection (Fig. 7A–E). Moreover, Western blot analysis showed that the levels of neurite markers were significantly lower in the midbrain of the kir6.2$^{-/-}$ mice than those in the WT mice. However, knockdown of the *Pm20d1* gene reversed the downregulation of the neurite markers in the midbrain of the kir6.2$^{-/-}$ mice (Fig. 7F and G). Similarly, Golgi staining indicated that the *Pm20d1* knockdown reversed the shortening of neurites and the decreased density of dendritic spines in the midbrain neurons of the kir6.2$^{-/-}$ mice (Fig. 7H–J). The above results revealed that *Pm20d1* knockdown significantly reversed the abnormal neurological features, including the impaired neuronal morphology, as well as motor and coordination disorders, in the kir6.2$^{-/-}$ mice.

3.8. *Kir6.2/KATP opener diazoxide elevates levels of synaptic proteins and enlarges neuronal processes in vivo*

As we found the regulatory effects of kir6.2 on the morphological maintenance of mesencephalic neurons in kir6.2$^{-/-}$ mice, we next asked whether pharmacological manipulation of kir6.2/KATP channel would play a role in these neurophysiological phenotypes. Age-related degeneration of neurons is reflected in several morphological changes, including axonal atrophy, decreases in neurite length and target innervation [14,28]. The kir6.2/KATP channel opener diazoxide is an FDA-approved drug for treating hypertension and hypoglycemia [29, 30]. To determine whether kir6.2/KATP channel is an important regulator of neurite morphology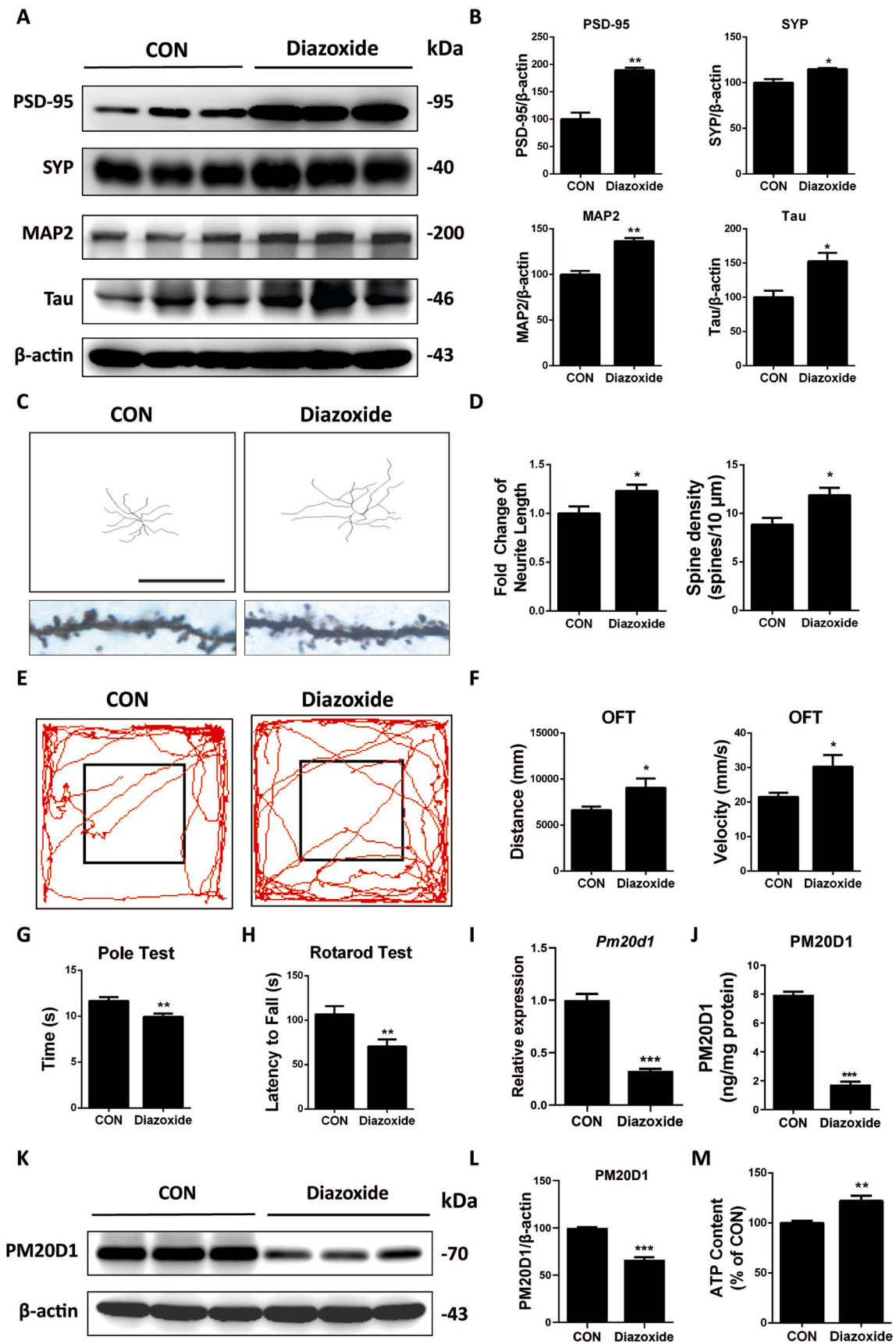 *in vivo*, aged mice were treated with diazoxide and then biochemical changes of mesencephalic neurons were detected. We found that the levels of neurite proteins were significantly higher in mesencephalic samples from diazoxide-treated mice compared to that of untreated mice (Fig. 8A and B). Consistent with these results, Golgi staining identified extended neurite length and increased spine density in the diazoxide-treated mice, shown in the representative ultrastructures of neurites under oil microscope and two-dimensional map of neurites (Fig. 8C and D). We also detected the effects of diazoxide on the voluntary movements of mice. Compared to the untreated aged mice, the diazoxide-treated mice showed a longer distance and faster speed in the OFT (Fig. 8E and F); and enhanced movement ability and improved motor coordination in the pole test and rotarod test (Fig. 8G and H). Importantly, these phenotypes were accompanied with decreased mRNA and protein levels of PM20D1 in the midbrain of diazoxide-treated mice (Fig. 8I-L). Diazoxide also counteracted the increased expression of PM20D1 (Fig. S5A-C), and increased ATP content (Fig. 8M) in the aged brain. These data collectively indicated that the use of kir6.2/KATP opener diazoxide exerted beneficial effects on neurites elongation and motor control, which supplementarily demonstrated the critical roles of kir6.2-composed KATP channel in morphological maintenance of neurons and domination of voluntary movement.

4. Discussion

In the present study, by analyzing the neurophenotypes of the kir6.2$^{-/-}$ mice, we found important roles of kir6.2 in maintaining the morphology of midbrain neurons and the motor coordination of mice. The underlying molecular mechanisms were deeply investigated by RNA-seq analysis, in which the *Pm20d1* gene was increased significantly in the midbrain of the kir6.2$^{-/-}$ mice. Further studies confirmed that PM20D1 secretase promoted the formation of endogenous mitochondrial uncoupling agents, leading to impaired neuronal processes *in vivo*. By knocking down *Pm20d1*, the abnormal neurite morphology and the impaired motor coordination in the kir6.2$^{-/-}$ mice were recovered. We demonstrated the importance of kir6.2 in the morphological maintenance of mesencephalic neurons. We also revealed the role of PM20D1 as a key factor leading to abnormal neurophenotypes of kir6.2-deficient mice (Graphical abstract).

Kir6.2 is widely distributed in the CNS but mainly resides in neurons [2,31,32]. As the most abundant cells in the brain, astrocytes only express kir6.2 under certain brain pathological states, including Alzheimer's disease (AD) and traumatic brain injury [3,4]. Our previous study has found that aberrantly-expressed kir6.2 in A1 astrocytes is a neurodegeneration propagator under inflammatory stress [21]. We confirm in the current study that kir6.2 is expressed specifically in neurons under physiological conditions, both *in vivo* and *in vitro*, which is consistent with former report [2].

Although kir6.2/KATP channels are distributed in peripheral tissues including pancreatic β cells, the basal levels of insulin secretion (at 2.8 mM glucose) and blood glucose levels in kir6.2$^{-/-}$ mice were not different from those in WT mice. Additionally, the basal level of glucose-dependent insulinotropic polypeptide (GIP) secretion in kir6.2$^{-/-}$ mice is considered to be maintained independently of the kir6.2/KATP channel. Therefore, it is rarely possible that neurites loss in kir6.2$^{-/-}$ mice is modulated by the neurotrophic effects of these metabolites [33,

A

B
PSD-95
SYP
MAP2
Tau

C

D

E

F
OFT
OFT

G
Pole Test

H
Rotarod Test

I
Pm20d1

J
PM20D1

K

L
PM20D1

M

(caption on next page)

Fig. 8. Kir6.2/KATP opener diazoxide elevates levels of synaptic proteins and enlarges neuronal processes *in vivo*.
(A) Immunoblotting analysis of neurite related markers including PSD95, SYP, MAP2, and Tau were detected in midbrain samples from diazoxide-treated and untreated mice. (B) Densitometric analysis of PSD-95, SYP, MAP2, and Tau in A. Data are represented as %. (C) Neuronal morphology in Golgi staining was reflected in a two-dimensional map generated by the Image J software (up). Scale bar is 200 μm. Dendritic spines photographed by oil microscope under 100x magnification (down). (D) Quantitative analysis of the average length of neuronal processes and the level of spine density in C. (E) Movement trace diagrams (red curve) of untreated and diazoxide-treated mice in the OFT. (F) Statistical charts of movement distance and moved speed in the OFT. (G) Analysis of the time consumed in pole test. (H) Analysis of latency time in the rotarod test. (I) *Pm20d1* mRNA in the midbrain of untreated and diazoxide-treated mice detected by RT-PCR. (J) Levels of PM20D1 in the midbrain of untreated and diazoxide-treated mice were determined by ELISA kit. (K) Immunoblotting analysis of PM20D1 in midbrain samples from diazoxide-treated and untreated mice. (L) Densitometric analysis of PM20D1 in K. Data are represented as %. (M) ATP contents in the midbrain of untreated and diazoxide-treated mice. Data are analyzed using unpaired Student's t-test. *$P < 0.05$, **$P < 0.01$ and ***$P < 0.001$ *vs.* CON group. Values are means ± SEM from 10 to 15 mice per group.. (For interpretation of the references to color in this figure legend, the reader is referred to the Web version of this article.)

34]. Kir6.2/KATP channels are also expressed on myocardial cells and vascular smooth muscle cells [1], however, we learned from the cardiac phenotypes of kir6.2 knockout animals that baseline ventricular action potential duration and contractile function are unaffected by kir6.2 deletion [35], implying that change of sarcolemmal kir6.2/KATP channels may not be so critical in physiological conditions of the CNS. Several studies have verified the critical roles of kir6.2/KATP channel in various neurons, including those of the cerebral cortex, substantia nigra, caudate and hippocampus. Kir6.2 is involved in the metabolic modulation of hypothalamic glucose-responsive neurons [36,37], the susceptibility of dopaminergic neurons in PD, and the electrical activity control of entorhinal cortex neurons [38,39]. Nonetheless, the neurological characteristics of *KCNJ11*-mutant patients and the behaviors of kir6.2$^{-/-}$ mice indicate that kir6.2 exerts significant but undervalued roles in the brain [5,40]. In our research, we found that kir6.2$^{-/-}$ mice exhibited reduced motor ability and impaired coordination, which corresponds to the hypoactivity observed clinically in patients with *KCNJ11* neonatal diabetes [5]. We also showed that kir6.2 deletion caused deficits in the morphological maintenance of midbrain neuronal processes. The midbrain is known to be responsible for exploratory behaviors [41,42]; however, in the current study, no significant change was found in the novel object recognition test. These results are consistent with the former study, which showed that KATP channels controlled the initiation of exploratory behaviors but did not affect the adaptive novelty-dependent behaviors [43].

The reduced complexity of neurites and the abnormal synaptic structure are closely related to behavioral disorders [44]. Dopamine-releasing midbrain neurons exhibit a large axonal tree and extensive synaptic arborizations, which are crucial for brain functions, including cognition, emotion, reward, as well as decision making and working memory [45]. We found the deficits in midbrain neurites and the impaired ability in voluntary movement of the kir6.2$^{-/-}$ mice, which may have a causal link between the two phenotypes. We conjecture that these deficits in neuronal morphology might have caused disruption of the electrophysiological activity or neurotransmission, thus directly causing the behavioral disorders in mice. Further research regarding the electrophysiological activity of mesencephalic neurons in kir6.2$^{-/-}$ mice is warranted. The highly complex structure of midbrain neurons is the basis of function, but also is the foreshadowing of its susceptibility from another point of view. As the extensively branched axonal domain imposes extraordinary metabolic costs on these cells, midbrain neurons are particularly vulnerable in Parkinson's disease [46]. In previous studies, kir6.2 deficiency recovered the pathological phenotypes of multiple mouse models for PD [38]. This occurrence can also be interpreted to be that kir6.2$^{-/-}$ mice reduce energy consumption by simplifying the complex structure of midbrain neurons, protecting the neurons from neurotoxic stress. In summary, reduced neurites in kir6.2$^{-/-}$ mice would impede movement control in the short run but could reduce metabolic demand in the long run. We further found the elevated effects of kir6.2/KATP channel opener diazoxide on neurite-related protein levels, which was consistent with previous studies confirming the biochemical correlation of diazoxide with increased levels of presynaptic proteins in mouse model for AD [29]. These studies collectively confirmed the cardinal roles of kir6.2 in the

CNS.

PM20D1 is a secreted enzyme that catalyzes the formation of N-AAAs from circulating fatty acids and amino acids in animals [23,47]. We demonstrated deletion of kir6.2 increased levels of N-AAAs. As mitochondrial uncoupling agents, these molecules dissociate the phosphorylation of ADP and oxidative metabolism to reduce ATP production [23]. Numerous studies have shown that induction of mitochondrial depolarization by mitochondrial uncouplers including carbonyl cyanide m-chlorophenylhydrazone (CCCP) or FCCP results in mitophagy-dependent degradation of the damaged mitochondria and reduced mitochondrial mass, subsequent to its uncoupling activity [48, 49]. We also observed in our study that the N-AAAs-treated primary neurons showed mitochondrial defects including reduced mitochondrial number and structural abnormalities. Whether mitophagy is involved in N-AAAs-induced mitochondrial loss and ATP shortage needs further investigation. Considering the inseparable correlations of mitochondrial multifaceted functions [50], N-AAAs-induced ATP shortage is more likely to be the collective failure of multiple mitochondrial functions. The brain is a high energy-consuming organ; thus, an ATP crisis may be detrimental, particularly to neurons. Studies have suggested that a decrease in ATP can potentially lead to neuronal degeneration and death [51], therefore, the non-apoptotic concentration of N-AAAs damaged the neurites in our *in vitro* experiments. It is also reported that systemic injection of N-AAAs produces behavioral signs in mice, such as increased immobility and reduced locomotor activity [51,52], which supports our notion that N-AAAs production induced by PM20D1 is the key factor leading to abnormal neurophenotypes of kir6.2$^{-/-}$ mice. In the present study, we showed that kir6.2 deletion promoted the upregulation of PM20D1 secretase in the midbrain and induced ATP shortage by producing the endogenous mitochondrial modulatory agents N-AAAs. This process led to the impaired neurite morphology and movement disorders under physiological circumstances.

Collectively, this study demonstrates the physiological function of kir6.2 in the morphological maintenance of neurons and motor coordination control of mice, which extends our understanding of KATP channels composed of kir6.2 in the CNS and provides insights into the pathological roles of kir6.2 in brain diseases.

Declaration of competing interest

The authors declare that they have no conflict of interest.

Acknowledgements

Appendix A. Supplementary data

Supplementary data to this article can be found online at https://doi.org/10.1016/j.redox.2021.102168.

Author contributions

Ethics statement

All animal experiments were approved by the Institutional Animal Care and Use Committee of Nanjing Medical University and complied with institutional guidelines.

Funding statement

References

[1] A. Tinker, Q. Aziz, Y. Li, M. Specterman, ATP-sensitive potassium channels and their physiological and pathophysiological roles, Comp. Physiol. 8 (4) (2018) 1463–1511.

[2] A. Thomzig, G. Laube, H. Pruss, R.W. Veh, Pore-forming subunits of K-ATP channels, Kir6.1 and Kir6.2, display prominent differences in regional and cellular distribution in the rat brain, J. Comp. Neurol. 484 (3) (2005) 313–330.

[3] C.M. Griffith, M.X. Xie, W.Y. Qiu, A.A. Sharp, C. Ma, A. Pan, et al., Aberrant expression of the pore-forming KATP channel subunit Kir6.2 in hippocampal reactive astrocytes in the 3xTg-AD mouse model and human Alzheimer's disease, Neuroscience 336 (2016) 81–101.

[4] L. Castro, M. Noelia, M. Vidal-Jorge, D. Sanchez-Ortizn, D. Gandara, E. Martinez-Saez, et al., Kir6.2, the pore-forming subunit of ATP-sensitive K(+) channels, is overexpressed in human posttraumatic brain contusions, J. Neurotrauma 36 (1) (2019) 165–175.

[5] P. Bowman, J. Day, L. Torrens, M.H. Shepherd, B.A. Knight, T.J. Ford, et al., Cognitive, neurological, and behavioral features in adults with KCNJ11 neonatal diabetes, Diabetes Care 42 (2) (2019) 215–224.

[6] C. Choeiri, W.A. Staines, T. Miki, S. Seino, J.M. Renaud, K. Teutenberg, et al., Cerebral glucose transporters expression and spatial learning in the K-ATP Kir6.2 (-/-) knockout mice, Behav. Brain Res. 172 (2) (2006) 233–239.

[7] X.R. Shi, J. Chang, J.H. Ding, Y. Fan, X.L. Sun, G. Hu, Kir6.2 knockout alters neurotransmitter release in mouse striatum: an in vivo microdialysis study, Neurosci. Lett. 439 (3) (2008) 230–234.

[8] A. Saito, K. Miyagawa, H. Miyagishi, K. Kurokawa, A. Umeda, Y. Okada, et al., Possible involvement of monoamine neurons in the emotional abnormality in Kir6.2-deficient mice, Physiol. Behav. 188 (2018) 251–261.

[9] P. Guedes-Dias, E. Holzbaur, Axonal transport: Driving synaptic function, Science 366 (6462) (2019).

[10] M.J. Devine, J.T. Kittler, Mitochondria at the neuronal presynapse in health and disease, Nat. Rev. Neurosci. 19 (2) (2018) 63–80.

[11] C. Bagni, R.S. Zukin, A synaptic perspective of fragile X syndrome and autism Spectrum disorders, Neuron 101 (6) (2019) 1070–1088.

[12] M.P. Forrest, E. Parnell, P. Penzes, Dendritic structural plasticity and neuropsychiatric disease, Nat. Rev. Neurosci. 19 (4) (2018) 215–234.

[13] M. Hick, U. Herrmann, S.W. Weyer, J.P. Mallm, J.A. Tschape, M. Borgers, et al., Acute function of secreted amyloid precursor protein fragment APPsalpha in synaptic plasticity, Acta Neuropathol. 129 (1) (2015) 21–37.

[14] N. Salvadores, M. Sanhueza, P. Manque, F.A. Court, Axonal degeneration during aging and its functional role in neurodegenerative disorders, Front. Neurosci. 11 (2017) 451.

[15] A. Bellucci, N.B. Mercuri, A. Venneri, G. Faustini, F. Longhena, M. Pizzi, et al., Review: Parkinson's disease: from synaptic loss to connectome dysfunction, Neuropathol. Appl. Neurobiol. 42 (1) (2016) 77–94.

[16] S. Dutta, P. Sengupta, Men and mice: relating their ages, Life Sci. 152 (2016) 244–248.

[17] J. Zhu, Z. Hu, X. Han, D. Wang, Q. Jiang, J.H. Ding, et al., Dopamine D2 receptor restricts astrocytic NLRP3 inflammasome activation via enhancing the interaction of beta-arrestin2 and NLRP3, Cell Death Differ. 25 (11) (2018) 2037–2049.

[18] X. Han, S. Sun, Y. Sun, Q. Song, J. Zhu, N. Song, et al., Small molecule-driven NLRP3 inflammation inhibition via interplay between ubiquitination and autophagy: implications for Parkinson disease, Autophagy 15 (11) (2019) 1860–1881.

[20] Y. Zhang, K. Chen, S.A. Sloan, M.L. Bennett, A.R. Scholze, S. O'Keeffe, et al., An RNA-sequencing transcriptome and splicing database of glia, neurons, and vascular cells of the cerebral cortex, J. Neurosci. 34 (36) (2014) 11929–11947.

[21] N. Song, H. Zhu, R. Xu, J. Liu, Y. Fang, J. Zhang, et al., Induced expression of kir6.2 in A1 astrocytes propagates inflammatory neurodegeneration via Drp1-dependent mitochondrial fission, Front. Pharmacol. 11 (2020) 618992.

[22] G.B. Bissonette, M.R. Roesch, Development and function of the midbrain dopamine system: what we know and what we need to, Gene Brain Behav. 15 (1) (2016) 62–73.

[23] J.Z. Long, A.M. Roche, C.A. Berdan, S.M. Louie, A.J. Roberts, K.J. Svensson, et al., Ablation of PM20D1 reveals N-acyl amino acid control of metabolism and nociception, Proc. Natl. Acad. Sci. U. S. A. 115 (29) (2018) E6937–E6945.

[24] J.Z. Long, K.J. Svensson, L.A. Bateman, H. Lin, T. Kamenecka, I.A. Lokurkar, et al., The secreted enzyme PM20D1 regulates lipidated amino acid uncouplers of mitochondria, Cell 166 (2) (2016) 424–435.

[25] B. Tan, D.K. O'Dell, Y.W. Yu, M.F. Monn, H.V. Hughes, S. Burstein, et al., Identification of endogenous acyl amino acids based on a targeted lipidomics approach, J. Lipid Res. 51 (1) (2010) 112–119.

[26] M. Connor, CW.Vandenberg RJ. Vaughan, N-acyl amino acids and N-acyl neurotransmitter conjugates: neuromodulators and probes for new drug targets, Br. J. Pharmacol. 160 (8) (2010) 1857–1871.

[27] A. Cheng, Y. Hou, M.P. Mattson, Mitochondria and neuroplasticity, ASN Neuro 2 (5) (2010), e00045.

[28] I.M. Parhad, J.N. Scott, L.A. Cellars, J.S. Bains, C.A. Krekoski, A.W. Clark, Axonal atrophy in aging is associated with a decline in neurofilament gene expression, J. Neurosci. Res. 41 (3) (1995) 355–366.

[29] D. Liu, M. Pitta, J.H. Lee, B. Ray, D.K. Lahiri, K. Furukawa, et al., The KATP channel activator diazoxide ameliorates amyloid-beta and tau pathologies and improves memory in the 3xTgAD mouse model of Alzheimer's disease, J Alzheimers Dis 22 (2) (2010) 443–457.

[30] S.V. Kharade, J.V. Sanchez-Andres, M.G. Fulton, E.L. Shelton, A.L. Blobaum, D. W. Engers, et al., Structure-activity relationships, pharmacokinetics, and pharmacodynamics of the kir6.2/SUR1-specific channel opener VU0071063, J. Pharmacol. Exp. Therapeut. 370 (3) (2019) 350–359.

[31] B. Liss, J. Roeper, Molecular physiology of neuronal K-ATP channels (review), Mol. Membr. Biol. 18 (2) (2001) 117–127.

[32] C. Karschin, C. Ecke, F.M. Ashcroft, A. Karschin, Overlapping distribution of K (ATP) channel-forming Kir6.2 subunit and the sulfonylurea receptor SUR1 in rodent brain, FEBS Lett. 401 (1) (1997) 59–64.

[33] T. Miki, K. Nagashima, F. Tashiro, K. Kotake, H. Yoshitomi, A. Tamamoto, et al., Defective insulin secretion and enhanced insulin action in KATP channel-deficient mice, Proc. Natl. Acad. Sci. U. S. A. 95 (18) (1998) 10402–10406.

[34] H. Ogata, Y. Seino, N. Harada, A. Iida, K. Suzuki, T. Izumoto, et al., KATP channel as well as SGLT1 participates in GIP secretion in the diabetic state, J. Endocrinol. 222 (2) (2014) 191–200.

[35] M. Suzuki, R.A. Li, T. Miki, H. Uemura, N. Sakamoto, Y. Ohmoto-Sekine, et al., Functional roles of cardiac and vascular ATP-sensitive potassium channels clarified by Kir6.2-knockout mice, Circ. Res. 88 (6) (2001) 570–577.

[36] D. Kong, L. Vong, L.E. Parton, C. Ye, Q. Tong, X. Hu, et al., Glucose stimulation of hypothalamic MCH neurons involves K(ATP) channels, is modulated by UCP2, and regulates peripheral glucose homeostasis, Cell Metabol. 12 (5) (2010) 545–552.

[37] A. Pocai, T.K. Lam, R. Gutierrez-Juarez, S. Obici, G.J. Schwartz, J. Bryan, et al., Hypothalamic K(ATP) channels control hepatic glucose production, Nature 434 (7036) (2005) 1026–1031.

[38] B. Liss, O. Haeckel, J. Wildmann, T. Miki, S. Seino, J. Roeper, K-ATP channels promote the differential degeneration of dopaminergic midbrain neurons, Nat. Neurosci. 8 (12) (2005) 1742–1751.

[39] M.S. Lemak, O. Voloshanenko, A. Draguhn, A.V. Egorov, KATP channels modulate intrinsic firing activity of immature entorhinal cortex layer III neurons, Front. Cell. Neurosci. 8 (2014) 255.

[40] R.M. Deacon, R.C. Brook, D. Meyer, O. Haeckel, F.M. Ashcroft, T. Miki, et al., Behavioral phenotyping of mice lacking the K ATP channel subunit Kir6.2, Physiol. Behav. 87 (4) (2006) 723–733.

[41] V. Caggiano, R. Leiras, H. Goni-Erro, D. Masini, C. Bellardita, J. Bouvier, et al., Midbrain circuits that set locomotor speed and gait selection, Nature 553 (7689) (2018) 455–460.

[42] A.J. Duszkiewicz, C.G. McNamara, T. Takeuchi, L. Genzel, Novelty and dopaminergic modulation of memory persistence: a tale of two systems, Trends Neurosci. 42 (2) (2019) 102–114.

[43] J. Schiemann, F. Schlaudraff, V. Klose, M. Bingmer, S. Seino, P.J. Magill, et al., K-ATP channels in dopamine substantia nigra neurons control bursting and novelty-induced exploration, Nat. Neurosci. 15 (9) (2012) 1272–1280.

[44] Y. Bai, M. Li, Y. Zhou, L. Ma, Q. Qiao, W. Hu, et al., Abnormal dendritic calcium activity and synaptic depotentiation occur early in a mouse model of Alzheimer's disease, Mol. Neurodegener. 12 (1) (2017) 86.

[45] E. Dragicevic, J. Schiemann, B. Liss, Dopamine midbrain neurons in health and Parkinson's disease: emerging roles of voltage-gated calcium channels and ATP-sensitive potassium channels, Neuroscience 284 (2015) 798–814.

[46] Y.C. Wong, R.A. Luk, K. Purtell, N.S. Burke, A.J. Stoessl, L.E. Trudeau, et al., Neuronal vulnerability in Parkinson disease: should the focus be on axons and synaptic terminals? Mov. Disord. 34 (10) (2019) 1406–1422.

[47] A. Saghatelian, Networking in circulation: lipoproteins, PM20D1, and N-acyl amino acid bioactivity, Cell Chem Biol 27 (9) (2020) 1112–1113.

[48] W. Springer, P.J. Kahle, Regulation of PINK1-Parkin-mediated mitophagy, Autophagy 7 (3) (2011) 266–278.

[49] N.D. Georgakopoulos, G. Wells, M. Campanella, The pharmacological regulation of cellular mitophagy, Nat. Chem. Biol. 13 (2) (2017) 136–146.

[50] J. Nunnari, A. Suomalainen, Mitochondria: in sickness and in health, Cell 148 (6) (2012) 1145–1159.

[51] Y. Moon, K.H. Lee, J.H. Park, D. Geum, K. Kim, Mitochondrial membrane depolarization and the selective death of dopaminergic neurons by rotenone: protective effect of coenzyme Q10, J. Neurochem. 93 (5) (2005) 1199–1208.

[52] H.B. Bradshaw, N. Rimmerman, J.F. Krey, J.M. Walker, Sex and hormonal cycle differences in rat brain levels of pain-related cannabimimetic lipid mediators, Am. J. Physiol. Regul. Integr. Comp. Physiol. 291 (2) (2006) R349–R358.